

# A Comprehensive Study of Gamma-Ray Burst Optical Emission:

## II. Afterglow Onset and Late Re-Brightening Components

En-Wei Liang<sup>1,2,3</sup>, Liang Li<sup>1</sup>, He Gao<sup>3</sup>, Bing Zhang<sup>3</sup>, Yun-Feng Liang<sup>1</sup>, Xue-Feng Wu<sup>4</sup>,  
Shuang-Xi Yi<sup>5</sup>, Zi-Gao Dai<sup>5</sup>, Qing-Wen Tang<sup>1</sup>, Jie-Min Chen<sup>1</sup>, Hou-Jun Lü<sup>3</sup>, Jin Zhang<sup>2,6</sup>,  
Rui-Jing Lu<sup>1</sup>, Lian-Zhong Lü<sup>1</sup>, and Jian-Yan Wei<sup>2</sup>

### ABSTRACT

We continue our systematic statistical study of various components in gamma-ray burst (GRB) optical lightcurves. We decompose the early onset bump and the late re-brightening bump with empirical fits and analyze their statistical properties. Among the 146 GRBs that have well-sampled optical lightcurves, the onset and re-brightening bumps are observed in 38 and 27 GRBs, respectively. It is found that the typical rising and decaying slopes for both the onset and re-brightening bumps are  $\sim 1.5$  and in  $\sim 1.15$ , respectively. No early onset bump in the X-ray band is detected to be associated with the optical onset bumps, while an X-ray re-brightening bump is detected for half of the re-brightening optical bumps. The peak luminosity is anti-correlated with the peak time,  $L_p \propto t_p^{-1.86 \pm 0.29}$  for the onset bumps and  $L_p \propto t_p^{-1.05 \pm 0.16}$  for the re-brightening bumps. Both  $L_p$  and the isotropic energy release of the onset bumps are correlated with  $E_{\gamma, \text{iso}}$ , whereas no similar correlation is found for the re-brightening bumps. These results suggest that the afterglow onset bumps are likely due to the deceleration of the GRB fireballs. Taking the onset bumps as probes for the properties of the fireballs and their ambient medium, we find that the typical power-law index of the relativistic electrons is 2.5 and the medium

---

<sup>1</sup>Department of Physics and GXU-NAOC Center for Astrophysics and Space Sciences, Guangxi University, Nanning 530004, China; lew@gxu.edu.cn

<sup>2</sup>National Astronomical Observatories, Chinese Academy of Sciences, Beijing, 100012, China

<sup>3</sup>Department of Physics and Astronomy, University of Nevada, Las Vegas, NV 89154; zhang@physics.unlv.edu

<sup>4</sup>Purple Mountain Observatory, Chinese Academy of Sciences, Nanjing 210008, China

<sup>5</sup>School of Astronomy and Space Science, Nanjing University, Nanjing, Jiangsu 210093, China

<sup>6</sup>College of Physics and Electronic Engineering, Guangxi Teachers Education University, Nanning, 530001, China

density profile behaviors as  $n \propto r^{-1}$  within the framework of the synchrotron external shock models. With the medium density profile obtained from our analysis, we also confirm the correlation between initial Lorentz factor ( $\Gamma_0$ ) and  $E_{\text{iso},\gamma}$  in our previous work. The jet component that produces the re-brightening bump seems to be on-axis and independent of the prompt emission jet component. Its kinetic energy budget would be comparable to the prompt emission component, but with a lower  $\Gamma_0$ , typically several tens.

*Subject headings:* radiation mechanisms: non-thermal — gamma-rays: bursts

## 1. Introduction

The understanding of the gamma-ray burst phenomenon has been greatly advanced in recent years. While the prompt gamma-ray emission is generally interpreted as due to internal dissipation processes within the relativistic ejecta due to internal shocks near or far above the photosphere (Rees & Mészáros 1994; Kobayashi et al. 1997; Daigne & Mochkovitch 1998; Rees & Mészáros 2005; Pe’er et al. 2006) or internal magnetic energy dissipation processes (e.g. Usov 1992; Thompson 1994; Drenkhahn & Spruit 2004; Giannios & Spruit 2006; Zhang & Yan 2011), the afterglow is usually interpreted as arising from the external shock formed as the fireball is decelerated by the ambient medium (Mészáros & Rees 1997; Sari et al. 1998).

In the pre-*Swift* era, afterglow observations were mostly made in the optical bands. The data were well explained by the external shock model (e.g., Mészáros & Rees 1997; Sari et al. 1998; Panaitescu et al. 1998; Panaitescu & Kumar 2001; Huang et al. 2000; see Zhang & Mészáros 2004 for review). The simultaneous observations with XRT and UVOT on board *Swift* (Gehrels et al. 2004) as well as ground-based optical telescopes in the early afterglow phase have opened a new window to understand GRB afterglow (Mészáros 2006; Zhang 2007; Liang 2010). In particular, early X-ray afterglow observations revealed erratic flares and early plateaus that are difficult to interpret within the standard theoretical framework (Zhang et al. 2006, Nousek et al. 2006). The flares are believed to be produced by late activities of the GRB central engine (Burrows et al. 2005; Fan & Wei 2005; Zhang et al. 2006; Dai et al. 2006; Proga & Zhang. 2006; Perna et al. 2006), and the shallow decay segment likely signals a long-lasting wind powered by the GRB central engine after the prompt gamma-ray phase (Dai & Lu 1998a,b; Zhang et al. 2006). These features indicate that the GRB central engine does not die out quickly. The observed afterglow emission is a superposition of the traditional external shock afterglow and an afterglow related to the late central engine activities (Zhang 2011).

The mix of various emission components makes afterglow lightcurves more diverse (e.g., Liang et al. 2008). One may decompose the lightcurves using two different approaches: one through theoretical modeling and the other through empirical fitting. Theoretical modeling prevailing in the pre-*Swift* era (e.g., Panaitescu et al. 1998; Panaitescu & Kumar 2001; Huang et al. 2000; Wu et al. 2005) is found increasingly difficult in the *Swift* era, because of the large amount of data, and more importantly, the chromatic behavior that defeats the simplest external shock model. We therefore take the more empirical approach to perform the analysis (e.g., Liang & Zhang 2006; Panaitescu & Vestrand 2008, 2011; Kann et al. 2010; 2011).

Our results are presented in a series of paper. In the first paper of this series (Li et al. 2012; paper I), we presented the general feature of a “synthetic” optical lightcurve based on our decomposition analysis. The “synthetic” optical lightcurve shows eight possible components with distinct physical origins (see Figure 2 of Paper I): these include prompt optical flares; an early optical flare of the reverse shock origin; an early shallow decay segment; the standard afterglow component (an onset hump followed by a normal decay decay segment); the post jet break phase; optical flares; a re-brightening hump; and a late supernova (SN) bump. The optical flares and the shallow decay segment may signal the late activities of the GRB central engine, which have been discussed in detail in Paper I. This paper is dedicated to the onset bump (component III) and the late re-brightening bump (component VI) in the synthetic lightcurve. The reason to discuss them together is because physically they share a similar origin of jet-medium interaction, and they would be good probes for the fireball and the ambient density profile (e.g., Liang et al. 2010; Lü et al. 2012; Ghirlanda et al. 2012; Yi et al. 2012).

The fireball model predicts a clear early onset hump in the afterglow lightcurve as the fireball is decelerated by the ambient medium (Rees & Mészáros 1992; Mészáros & Rees 2003; Sari & Piran 1999 for the thin shell case, and Kobayashi et al. 1999; Kobayashi & Zhang 2007 for the thick shell case). The epoch of deceleration depends on the energy of the fireball, density of the medium, and more sensitively the initial Lorentz factor of the ejecta,  $\Gamma_0$ . The slopes of the onset bumps are determined by both the medium density profile (the  $k$  value by assuming  $n \propto r^{-k}$ ) and the electron spectral index,  $p$ . Therefore, the afterglow onset bumps would be an ideal probe to study the properties of the fireball and the circumburst medium. The re-brightening feature is likely related to another emission component, and hence, may probe the jet structure. We present the data and lightcurve fitting results in §2 and compare the properties of the onset and late re-brightening bumps in §3. We measure  $\Gamma_0$ ,  $p$ , and  $k$  with the onset bumps in §4. An analysis for the physical origin of the re-brightening bumps is presented in §5. A summary and discussion of our results are presented in §6. Throughout, the physical parameters are in cgs units and the

notation  $D_n$  is for  $D/10^n$ .

## 2. Data and Lightcurve Fitting

All the GRBs that have optical afterglow detections by November 2011 (from Feb. 28 1997 to Nov. 2011) are included in our analysis. A sample of 225 optical lightcurves are compiled from published papers, or from GCN Circulars if no published paper is available. Well-sampled lightcurves are available for 146 GRBs. The sample has been presented in Table 1 of Paper I, in which GRB name, redshift, optical spectral information, observational time interval, as well as  $\gamma$ -ray spectral parameters are summarized (Li et al. 2012). We collected the optical spectral indices  $\beta_O$  (defined with the convention  $F_\nu \propto \nu^{-\beta_O}$ )<sup>1</sup> and the host galaxy extinction  $A_V$  for each burst from the same literature in order to reduce the uncertainties introduced by different authors. Galactic extinction correction is made by using a reddening map presented by Schlegel et al. (1998). Since the  $A_V$  values are available only for some GRBs and the  $A_V$  is derived from the spectral fits using different extinction curves, we do not make correction for the GRB host galaxy extinction. The  $k$ -correction in magnitude is calculated by  $k = -2.5(\beta_O - 1) \log(1 + z)$ . For late epoch data ( $\sim 10^6$  seconds after the GRB triggers), a possible flux contribution from the host galaxy is subtracted. The isotropic gamma-ray energy ( $E_{\gamma, \text{iso}}$ ) is derived in the rest frame  $1 - 10^4$  keV energy band using the spectral parameters. We fit the lightcurves with a model of multiple power-law components. The basic component of our model is either a power-law function,  $F = F_0 t^{-\alpha}$  or a smooth broken power-law function,  $F = F_0 [(t/t_b)^{\alpha_1 \omega} + (t/t_b)^{\alpha_2 \omega}]^{-1/\omega}$ , where  $\alpha$ ,  $\alpha_1$ ,  $\alpha_2$  are the temporal slopes,  $t_b$  is the break (or peak) time, and  $\omega$  measures the sharpness of a break (or peak) of the lightcurve component. In some cases, we adopt a tripple broken-power-law model. We developed an IDL code to make best fits with a subroutine called MPFIT<sup>2</sup>. For the details of our lightcurve fitting, see Paper I.

As shown in Paper I, eight components are decomposed from the observed optical lightcurves. This paper focuses on the early afterglow onset and late re-brightening afterglow components. The reason to discuss them together is because they may be both related to a similar physical origin, i.e., multiple fireball components are decelerated by the circum-burst medium viewing from different or same angles from the jet axes. An afterglow onset feature is characterized by a smooth bump with a peak less than 1 hour post trigger, which is followed by a normal (decay index between -0.75 and -2) power-law decay compo-

---

<sup>1</sup>An optical spectral index  $\beta_O = 0.75$  is adopted for those GRBs whose  $\beta_O$  is not available.

<sup>2</sup><http://www.physics.wisc.edu/~craigm/idl/fitting.html>.

ment. A rebrightening bump is similar to an onset bump but peaks at a much later time. The supernova bump is a special late rebrightening peaking at around 1-2 weeks after a GRB trigger, which usually shows a red color. We exclude the supernovae bumps in this analysis by restricting the peak time of the bumps to be earlier than 7 days after a GRB trigger. Throughout, we mark the parameters of the early onset bumps and the late re-brightening bumps with the superscripts “on” and “re”, respectively. We classify the optical lightcurves with the detections of an onset bump and/or a late re-brightening bump into four groups as described below.

- Group I: This group includes bursts with an onset bump followed by a normal decay segment without a late re-brightening bump, as shown in Figure 6. These are a textbook version of lightcurves as predicted by the standard fireball model. Erratic flares are superimposed in the lightcurves of some lightcurves, but they may be produced by late internal shocks as presented in paper I. We have 26 cases in the current sample.
- Group II: This group includes bursts with an initial afterglow onset bump followed by a late re-brightening hump. We have 12 cases in the current sample. They are shown in Figure 2
- Group III: This group includes bursts with an initial shallow decay segment followed by a late re-brightening hump. We have 8 cases in the current sample (Figure 3)
- Group IV: This group includes bursts with an initial normal decay followed by a late re-brightening bump. We have 7 cases in the current sample (Figure 4).
- Group V: This group includes bursts with a bump peaking at  $> 10^4$  seconds post the GRB trigger. We have 3 cases (GRBs, 060614, 070306 and 100418) in the current sample (Figure 5).

Altogether we get 38 early afterglow onset bumps<sup>3</sup> and 27 late re-brightening bumps for our statistical analysis. The lightcurve fitting parameters and the observational information of GRBs are reported in Tables 1 and 2 for the afterglow onset bump sample and the late re-brightening bump sample, respectively.

---

<sup>3</sup> An early onset bump may be also embedded in the data of GRBs 080319A and 090716 with our lightcurve fits. However, the bumps are highly contaminated with bright flares or reversed shock emission. The rising slopes are very uncertain. We therefore do not include these bumps in our sample.

### 3. Comparison between the Properties of the Early Onset and Late Re-Brightening bumps

We compare the distributions of  $\alpha_1$ ,  $\alpha_2$ ,  $t_p$ , the R-band luminosity at  $t_p$  ( $L_{R,p}$ ) and the ratio ( $R_{td}$ ) of rising-to-decaying timescales measured at the full-width-half-maximum (FWHM) in Figure 6. It is found that both  $\alpha_1^{\text{on}}$  and  $\alpha_1^{\text{re}}$  distributions are well consistent with each other, falling in the range of  $0.3 \sim 4$ , with a typical value 1.5. Both  $\alpha_2^{\text{on}}$  and  $\alpha_2^{\text{re}}$  are also consistent. They are narrowly distributed in the range of  $0.6 \sim 1.8$  with a typical value  $\sim 1.15$ , except for three outliers whose  $\alpha_2^{\text{re}}$  are steeper than 2. The distribution of the ratio  $R_{td}$  is clustered around  $\sim 0.4$ . While  $t_p^{\text{on}}$  is distributed in the range from 30 to 3000 seconds,  $t_p^{\text{re}}$  is distributed in a much wider range from several hundreds of seconds to days. The  $L_{R,p}^{\text{on}}$  distribution shows a bimodal feature that peaks at  $10^{46}$  erg s $^{-1}$  and  $10^{48}$  erg s $^{-1}$ , respectively, but this feature is still not statistically significant in the current sample<sup>4</sup>. A sharp cutoff at the left side of the first peak is likely due to an instrumental detection limit, which selects against faint optical afterglow onset bumps. The log-normal function fit to the  $L_{R,p}^{\text{re}}$  distribution yields  $\log L_{R,p}^{\text{re}} = 45.76 \pm 0.90$  ( $1\sigma$ ).

Figure 7 shows the width and peak luminosity as a function of the peak time for both the onset and re-brighten bumps. It is found that they share the same  $w - t_p$  relation, i.e.,  $\log w = (0.38 \pm 0.14) + (0.96 \pm 0.03) \log t_p$  with a Spearman correlation coefficient  $r = 0.96$ . The peak luminosity is anti-correlated with the peak time for both the onset and re-brightening bumps, but the power-law indices of the correlations are different. The best fits give  $\log L_{R,p,47}^{\text{on}} = (2.89 \pm 0.62) - (1.86 \pm 0.29) \log t_p^{\text{on}}/(1+z)$  (with  $r = 0.75$ ,  $p < 10^{-4}$ ) and  $\log L_{R,p,47}^{\text{re}} = (1.61 \pm 0.60) - (1.05 \pm 0.16) \log t_p^{\text{re}}/(1+z)$  (with  $r = -0.82$ ,  $p < 10^{-4}$ ). Both onset and re-brightening bumps are detected for 12 GRBs. We check the correlation between their peak luminosities, but no correlation is found, which is shown in Figure 8.

The correlation between the peak luminosity and isotropic gamma-ray energy for both the onset and re-brightening bumps are shown in Figure 9. It is found that  $L_{p,R}^{\text{on}}$  is tightly correlated with  $E_{\gamma,\text{iso}}$ . The best fit gives  $\log L_{p,R,48}^{\text{on}} = (3.77 \pm 0.43) + (1.00 \pm 0.14) \log E_{\gamma,\text{iso},50}$  ( $r = 0.79$ ,  $p = 10^{-4}$ ). We derive the isotropic energy release in the  $R$  band ( $E_{R,\text{iso},50}$ ) for the afterglow onset and re-brightening bumps in the time interval  $[t_p/5, 5t_p]$ . The parameter  $E_{R,\text{iso}}^{\text{on}}$  is also correlated with  $E_{\gamma,\text{iso}}$  ( $r = 0.71$ ,  $p < 10^{-4}$ ). However, we do not find similar

---

<sup>4</sup>Since the visual bimodal distribution feature depends on the bin size selection, we examined this feature with a statistical algorithm proposed by Keith et al. (1994), the so-called KMM algorithm, which is independent of bin size selection effect. The KMM algorithm yields a likelihood ratio test statistics ( $r$ ) and a corresponding chance probability  $p^{\text{KMM}}$ . A bimodal feature is statistically acceptable if  $p < 10^{-4}$ . We get  $r = 2.2$  and  $p = 0.33$ , which means that the bimodal feature is still not statistically acceptable.

correlations for the late re-brightening bumps in the current sample. The luminosity  $L_{\text{p,R}}^{\text{re}}$  is usually smaller than  $L_{\text{p,R}}^{\text{on}}$ , but the energy  $E_{\text{R,iso}}^{\text{re}}$  is comparable to  $E_{\text{R,iso}}^{\text{on}}$ .

Both X-ray and optical afterglows were observed for most GRBs in our sample. The X-ray afterglow lightcurves observed with *Swift*/XRT are also shown in Figures 1-5. We check whether an onset or re-brightening bump also exists in the X-ray lightcurve at the time of optical onset/rebrightening bumps. For the onset bumps, the X-ray lightcurves are usually characterized by a steep decay segment or flares. No associated onset bumps are identified detected (see Figure 1)<sup>5</sup>. For the re-brightening bumps, on the other hand, the associations seem common. A simultaneous bump in the X-ray band is detected in about half of the optical re-brightening bumps (Figure 2). These results suggest that the optical lightcurves are less contaminated by the prompt emission tail and late central engine activity emission, and therefore a good probe for the external shock afterglow.

#### 4. Onset bumps: Probing properties of fireball and circumburst medium density profile

Within the framework of the synchrotron external shock model, a clear onset bump is expected in the early afterglow lightcurve (e.g., Sari & Piran 1999). The tight  $L_{\text{p,R}}^{\text{on}} - E_{\gamma,\text{iso}}$  correlation and the values of the rising and decay slopes are all consistent with the model that invokes early deceleration of the GRB fireball<sup>6</sup>. In this section we take the deceleration model to interpret the onset bumps, and use the data to probe the properties of fireball and circumburst medium density profile.

---

<sup>5</sup>The decay slope post the onset peak is roughly consistent with that observed in the X-ray band for GRBs 060418, 061007, 061121, 071010B, 071025, 071031, 071112C, 080603A, 080810, 081008, 081109A, 081203A, 090812, 110205A, 070318, 080310, 070411, 080710, 090102, 100901, 060729, 081029, 100219A. The early afterglow onset bump in the X-ray band, if exist, would be highly contaminated by the early steep decay segment and flares. Therefore, the onset bump is difficult to identified in the X-ray band.

<sup>6</sup>A smooth bump may be also attributed to an off-axis viewing angle effect (Panaitescu & Vestrand 2008). In this case the rising part of the bump is defined by the off-beam effect, while the decaying part would correspond to the post jet break deceleration phase (with a decay slope steeper than 1.5). However, the majority of  $\alpha_2$  in our sample is shallower than 1.5 (see also Liang et al. 2010).

#### 4.1. Circumburst medium density profile and electron spectral index

The rising and decaying slopes of an afterglow onset bump depend on the circumburst medium density profile parameter  $k$  and the radiation spectral regime. As shown in Table 1 of Paper I, the spectral index for most optical afterglows are between 0.5-0.7, indicating that the optical emission is usually in the spectral regime  $\nu_m < \nu < \nu_c$  and  $p > 2$ , where  $\nu_m$  and  $\nu_c$  are the typical and cooling frequencies of synchrotron radiation. Within the deceleration model, the rising and decaying slopes of the onset bump depend on the circumburst medium density profile (e.g. Xue et al. 2009). For  $\nu_m < \nu_O < \nu_c$  and  $p > 2$ , the rising and decaying slopes are 3 and  $3(1-p)/4$ , respectively, for the constant density ISM model, and are  $(1-p)/2$  and  $(1-3p)/4$ , respectively, for the wind model. For typical values (e.g.  $p = 2.3$ ), the predicted values are significantly inconsistent with the observed values. The rising slopes disfavor both the ISM medium and the wind medium for most GRBs.

We consider a general circumburst medium density profile

$$n = \begin{cases} n_0 \left(\frac{R}{R_t}\right)^{-k}, & R \leq R_t, \\ n_0, & R > R_t, \end{cases} \quad (1)$$

where  $R_t$  is the transition radius at which the medium turns into a constant density ISM. The thin-shell external shock model gives the rising slope

$$\alpha_1 = 3 - \frac{k(p+5)}{4}. \quad (2)$$

Since the decaying phase after the bump usually lasts a much longer time, it is likely that the blastwave has passed  $R_t$  soon after reaching the peak, and the long-term decay slope is defined by the constant-density ISM scaling<sup>7</sup>, i.e.

$$\alpha_2 = -\frac{3(p-1)}{4}. \quad (3)$$

With the observed  $\alpha_1$  and  $\alpha_2$  one can derive the  $k$  and  $p$  values for each burst. We find that 36 out of the 42 bursts in our sample can be explained with this simple model. Six GRBs cannot be explained with this model. The early bumps in GRBs 090102, 110205, and 110906 have a very rapid rising with an index 5.22, 4.00, and  $3.4 \pm 0.23$ , respectively. This may be due to the contamination of the reversed shock emission (e.g., Zhang et al. 2003, Zheng et

---

<sup>7</sup>It is also possible that the medium profile transits to the wind medium since the radius of the wind medium would be  $> 10^{19}$  cm in some GRBs (e.g. Dai & Wu 2003). In this case the decay slope  $\alpha_2 = (1-3p)/4$ .



al. 2012). The decay slope of the bumps in GRBs 030418, 071010B and 081126, on the other hand, are too shallow ( $0.55 \pm 0.04$ ,  $0.60 \pm 0.06$ ,  $0.39 \pm 0.01$ , respectively) to be interpreted in the standard fireball model, and requires significant energy injection<sup>8</sup>. We therefore only include 36 GRBs in our following analysis.

Figure 10 shows the distributions of  $p$  and  $k$ . The  $p$  values range from 2 to 3.5, with a typical value of 2.5. Both analytical and numerical studies show that the spectrum of electrons accelerated by ultra-relativistic shocks are a power-law with an index in this range (Kirk et al. 2000, Achterberg et al. 2001, Bednarz & Ostrowski 1998, Lemonine & Pelletier 2003). The derived  $p$  values from our analysis are generally consistent with this, but they are distributed in a wider range (see also Shen et al. 2006).

The  $k$  values vary from 0 to 1.5 among GRBs, and its typical value is 1. Most of them are narrowly distributed in the range 0.75 – 1.25. This is an intermediate regime between ISM and stellar wind. It may be formed via episodic energy ejection of matter by the progenitor star some time before the GRB. The exact mechanism to shape such a density profile is subject to further theoretical study.

## 4.2. Relation between Fireball Lorentz Factor and Isotropic Gamma-ray Energy

Liang et al. (2010) derived the initial Lorentz factor  $\Gamma_0$  and  $R_{\text{dec}}$  assuming that the early optical afterglow onset bumps are due to the deceleration of a GRB fireball in an ISM medium, and discovered a tight correlation between  $\Gamma_0$  and  $E_{\gamma, \text{iso}}$ . We revisit this relation in view of the modified density profile as discussed above. We define a dimensionless parameter

$$\xi \equiv \frac{R_t}{R_{\text{dec, cr}}}, \quad (4)$$

where  $R_{\text{dec, cr}}$  is the deceleration radius of the GRB fireball in the ISM model, which can be calculated by

$$R_{\text{dec, cr}} = 2.0 \times \left[ \frac{3E_{\gamma, \text{iso}} t_p}{32\pi\eta n m_p c(1+z)} \right]^{\frac{1}{4}}, \quad (5)$$

where  $n$  is the ambient density and  $\eta = E_{\gamma, \text{iso}}/E_{\text{K, iso}}$  is the ratio between the isotropic gamma-ray energy and the isotropic blastwave kinetic energy,  $m_p$  is the mass of proton,  $c$  speed of

---

<sup>8</sup>We should note that the lightcurves of GRBs 030418, 071010B and 081126, are poorly sampled or only are covered for a short time interval.

light. In the moderate density profile  $n = n_0 r^{-k}$  as we derived above, the deceleration radius should be

$$R'_{\text{dec}} = \left[ \frac{(3-k)E_{\gamma,\text{iso}}}{2\pi\eta n_0 \xi^k R_{\text{dec,cr}}^k m_p \Gamma_0^2 c^2} \right]^{\frac{1}{3-k}}. \quad (6)$$

The initial Lorentz factor can be then estimated with<sup>9</sup>

$$\Gamma'_0 = \begin{cases} G(k) \times \left[ \frac{(3-k)E_{\gamma,\text{iso}}(1+z)^{3-k}}{32\pi\eta n_0 \xi^k R_{\text{dec,cr}}^k m_p c^{5-k} t_p^{3-k}} \right]^{\frac{1}{8-2k}}, & \xi \gg 1 \\ 1.4 \times \left[ \frac{3E_{\gamma,\text{iso}}(1+z)^3}{32\pi\eta n_0 m_p c^5 t_p^3} \right]^{\frac{1}{8}}, & \xi \ll 1, \end{cases} \quad (7)$$

where  $G(k)$  is a dimensionless parameter, which is a function of  $k$  as shown in Figure 11. We take  $n_0 = 1 \text{ cm}^{-3}$ ,  $\eta = 0.2$  and  $\xi = 3$  to calculate  $\Gamma_0$  and  $R'_{\text{dec}}$ . The distributions of the derived  $\Gamma'_0$  and  $R'_{\text{dec}}$  are shown in Figure 12. It is found that  $\Gamma'_0$  is distributed in the range 50 – 500, and  $R'_{\text{dec}}$  is narrowly clustered around  $10^{17} \text{ cm}$ . The relation between  $\Gamma'_0$  and  $E_{\text{iso}}$  is shown in Figure 13. The best fit yields

$$\log \Gamma'_0 = (1.43 \pm 0.10) + (0.26 \pm 0.03) \log E_{\text{iso},50}, \quad (8)$$

or  $\Gamma'_0 = (27 \pm 6) E_{\text{iso},50}^{0.26 \pm 0.03}$ . The slope of this relation is consistent with that reported in Liang et al. (2010), but the constant term is smaller since here we adopt the density profile as discussed above and replace the constant factor 2 by 1.4 in our calculation of the initial Lorentz factor.

## 5. Re-brightening Bumps: possible origins

As summarized in §2, late rebrightening bumps are observed in 27 GRBs. Several models may produce a rebrightening bump, including a medium density jump (Dai & Lu 2002; Dai & Wu 2003; Lazzati et al. 2002), a refreshed shock (Zhang & Mészáros 2002a; Björnsson et al. 2004); a structured jet (Nakar et al. 2003; Berger et al. 2003; Huang et al. 2004; Liu et al. 2006; Jia et al. 2012), and emission from a long-lived reverse shock due to certain stratified ejecta profile (Uhm et al. 2012). A density bump is difficult to produce very sharp rebrightenings (Nakar & Granot 2007). The refreshed shock scenario requires a large total energy budget to be at least comparable to the existing energy in the blastwave, even

---

<sup>9</sup>The constant factor 2 shown in Sari & Piran (1999) is replaced by 1.4 through rigorous integration, as suggested by Lü et al. 2012.

though a reverse shock can be bright enough to power a rapid optical rebrightening feature (Zhang & Mészáros 2002a). The long-lasting reverse shock model (Uhm et al. 2012) needs to have the forward shock suppressed in order to have a significant rebrightening feature from the reverse shock.

In the following we focus on the structured jet model. Three scenarios involving structured jets may be employed to explain the late re-brightening bumps. First, the outflow may have two components with different jet axis. The on-axis one gives rise to the prompt emission and early afterglow, while the off-axis one enters the field of view at a later time and gives the re-brightening feature (e.g. Granot et al. 2002). This model interprets the rebrightening bump as the full emergence of the off-axis jet in the field of view (Huang et al. 2004; Panaitescu & Vestrand 2008; Guidorzi et al. 2009, Margutti et al. 2010). This requires a uniform jet with a sharp edge, with the light of sight initially outside the jet cone. The peak of the bump corresponds to the epoch when the  $1/\Gamma$  cone enters the line of sight, i.e.,  $(\theta_v - \theta_j) = 1/\Gamma$ , where  $\theta_v$  and  $\theta_j$  are the viewing angle and the jet opening angle, respectively. This model predicts that the rising index of the lightcurve is steep, i.e.  $\alpha_1^{\text{re}} \sim (3 - 4)$  (Panaitescu & Vestrand 2008). However, as shown in Figure 6, the  $\alpha_1$  values for most late re-brightening bumps are  $\leq 3$ . The decaying part of the bumps in the off-axis scenario should correspond to the post jet break phase, which should be steeper than 1.5 (e.g., Liang et al. 2008). However, the majority of  $\alpha_2^{\text{re}}$  in our sample is shallower than 1.5. All these suggest that the off-axis two-component jet model is not supported by the data of majority GRBs that show a rebrightening bump.

The second model invokes a structured jet with smoothly varying energy per solid angle, usually as a power law or Gaussian distribution (e.g. Mészáros et al. 1998; Zhang & Mészáros 2002b; Rossi et al. 2002). For the Gaussian model (e.g. Zhang et al. 2004), an off-axis observer at a large viewing angle would see a smooth rebrightening feature (Granot & Kumar 2003). However this feature is too mild to interpret the observed rebrightening bumps in our sample.

The third model invokes two on-axis jets with different opening angles and Lorentz factors, with the fast one powering the prompt emission and early afterglow onset and the slow one powering the rebrightening bump (e.g. Racusin et al. 2008). This is likely the best model to interpret the rebrightening bumps. Since the rebrightening is interpreted as deceleration of the second slow jet, the rising and decaying slopes and the  $t_r/t_d$  ratio should be similar to those of the onset bumps<sup>10</sup>. This is indeed the case, as shown in Figure

---

<sup>10</sup>An issue may be that the circumburst medium is already modified by the first fireball, so that the second component is traveling in a cleared medium. This can be alleviated if the  $1/\Gamma$  cone of the slow jet is wider

6. On the other hand, the properties of the re-brightening humps are not correlated with the prompt gamma-ray properties. This suggests that the slow component responsible for the re-brightening bump is likely an independent component that is not related to the prompt gamma-ray emission.

One may estimate the initial Lorentz factor of the slow component if it is decelerated by the same medium as the fast component. The emission in the re-brightening component should be in the spectral regime  $\nu_m < \nu_X < \nu_c$ . The observed flux thus could be (e.g., Sari et al. 1998),

$$F \propto E_K^{(p+3)/4}, \quad (9)$$

where  $E_k$  is the kinetic energy of the slow component. Assuming that the microphysical parameters in the two components are the same, one can estimate the ratio of  $E_K$  for the two components

$$\frac{E_K^{\text{re}}}{E_K^{\text{on}}} = \left( \frac{F^{\text{re}}}{F^{\text{on}}} \right)^{4/(p+3)}. \quad (10)$$

Therefore, the ratio of the initial Lorentz factors of the two jet components can be estimated as

$$\frac{\Gamma_0^{\text{re}}}{\Gamma_0^{\text{on}}} = \left( \frac{F^{\text{re}}}{F^{\text{on}}} \right)^{1/(2p+6)} \left( \frac{t_p^{\text{on}}}{t_p^{\text{re}}} \right)^{3/8}. \quad (11)$$

Taking a typical value  $p = 2.3$ , one can see that the ratio is insensitive to the flux ratio. For typical values of  $t_p^{\text{on}} \sim 200\text{s}$  and  $t_p^{\text{re}} \sim 5 \times 10^4\text{s}$ , one gets typically  $\Gamma_0^{\text{re}} \sim 25$  for  $\Gamma_0^{\text{on}} \sim 200$ .

## 6. Conclusions

We have presented a detailed analysis of the optical afterglow onset and late re-brightening bumps with a sample of 146 well-sampled optical lightcurves. We made empirical fits to the lightcurves to identify these bumps and studied the statistical properties of various parameters. We summary our results in the following.

- A smooth onset bump is observed in 38 GRBs. Among them 26 show a clear onset feature followed by a normal decay segment without detection of a late re-brightening bump, while 12 others are followed by a late re-brightening hump. Sixteen GRBs in our sample show a power-law decay segment followed by a late re-brightening hump. No X-ray onset bump was observed to coincide the optical onset bumps in our sample.

---

than the narrow jet.

However, an associated X-ray re-brightening bump was detected for half of the optical re-brightening bumps.

- The distributions of  $\alpha_1$  and  $\alpha_2$  of both the onset and re-brighten bumps are consistent with each other. The  $\alpha_1$  distribution is in the range of  $0.3 - 4$  with a typical values of  $\sim 1.5$ , while  $\alpha_2$  is narrowly distributed in the range of  $0.6 - 1.8$  with a typical values  $\sim 1.15$ . The distribution of the ratio  $R_{td}$  is clustered around 0.4. The  $t_p^{on}$  distribution ranges from 30 to 3000 seconds, while  $t_p^{re}$  is distributed in a much wider range from several hundreds of seconds to days.
- Both the onset and re-brighten bumps share the same width-peak luminosity relation, i.e.,  $\log w = (0.38 \pm 0.14) + (0.96 \pm 0.03) \log t_p$ , indicating that a bump peaking earlier tends to be wider. The peak luminosity is anti-correlated with the peak time for both the onset and re-brightening bumps, but the power-law indices of the correlations are different, i.e.,  $-1.86 \pm 0.29$  for the onset bumps and  $-1.05 \pm 0.16$  for the re-brightening bumps. No correlation between the peak luminosities of the onset and re-brighten bumps is found.
- It is found that  $L_{p,R}^{on}$  is proportional to  $E_{\gamma,iso}$ , i.e.,  $\log L_{p,R,48}^{on} = (3.77 \pm 0.43) + (1.00 \pm 0.14) \log E_{\gamma,iso,50}$ , and the isotropic energy release during in the onset bump is also correlated with  $E_{\gamma,iso}$ . These results indicate that the afterglow onset bumps is likely due to the deceleration of the GRB fireballs.
- We take the onset bumps as a probe for the properties of the GRB fireball and the circumburst medium density profile. We find that the electron spectral index  $p$  is distributed in the range from 2 to 3.5 among bursts, with a typical value of 2.5. The medium density profile is characterized by  $n \propto r^{-k}$ , with the  $k$  values narrowly distributed in the range of  $0.75 - 1.25$ , with a typical value  $k = 1$ . This profile is intermediate between a constant density ISM and a stellar wind. The physical origin of this profile is subject to further study. With this medium density profile, we re-derive the initial Lorentz factor of the fireball and confirm the  $\Gamma_0 - E_{iso,\gamma}$  correlation discovered in our previous work (Liang et al. 2010).
- The peak time and peak luminosity of the rebrightening bumps are not correlated with the properties of the prompt gamma-ray emission and those of the onset bumps. Their rising and decaying slopes are not consistent with the prediction of off-axis two-component jet models. Rather, it seems to be consistent with an on-axis two-component jet model, with the rebrightening bump signaling the slow component. Within this interpretation, the slow component have a kinetic energy comparable to the fast component that is responsible for the prompt emission and onset afterglow

component. Its initial Lorentz factor is typically only a few tens, being much smaller than that of the fast component.

Our results indicate that the optical afterglow is a critical probe for the GRB external shock. Inspecting the X-ray lightcurves in Figure 1-5, one can find that the early X-ray afterglow lightcurves are usually dominated by flares and the tail emission of prompt gamma-rays. The optical afterglow lightcurves are much less contaminated by these emission components. The smooth onset bumps are a clean probe of the key parameters of the fireball and circumburst medium density profile.

We acknowledge the use of the public data from the Swift data archive. This work is supported by the “973” Program of China (2009CB824800), the National Natural Science Foundation of China (Grants No. 11025313, 11203008, 11078008, 11063001, 11163001, 11033002), Special Foundation for Distinguished Expert Program of Guangxi, the Guangxi Natural Science Foundation (2010GXNSFA013112, 2011GXNSFB018063 and 2010GXNSFC013011), the special funding for national outstanding young scientist (Contract No. 2011-135), and the 3th Innovation Project of Guangxi University. BZ acknowledges support from NSF (AST-0908362).

## REFERENCES

- Achterberg, A., Gallant, Y. A., Kirk, J. G., & Guthmann, A. W. 2001, MNRAS, 328, 393
- Antonelli, L. A., Testa, V., Romano, P., et al. 2006, A&A, 456, 509
- Bednarz, J., & Ostrowski, M. 1998, Physical Review Letters, 80, 3911
- Berger, E., Kulkarni, S. R., Pooley, G., et al. 2003, Nature, 426, 154
- Björnsson, G., Gudmundsson, E. H., & Jóhannesson, G. 2004, ApJ, 615, L77
- Burrows, D. N., Romano, P., Falcone, A., et al. 2005, Science, 309, 1833
- Cenko, S. B., Kasliwal, M., Harrison, F. A., et al. 2006, ApJ, 652, 490
- Cenko, S. B., Kelemen, J., Harrison, F. A., et al. 2009, ApJ, 693, 1484
- Cenko, S. B., Frail, D. A., Harrison, F. A., et al. 2011, ApJ, 732, 29
- Chester, M. M., Wang, X. Y., Cummings, J. R., et al. 2008, American Institute of Physics Conference Series, 1000, 421

- Covino, S., D’Avanzo, P., Klotz, A., et al. 2008, MNRAS, 388, 347
- Cucchiara, A., Cenko, S. B., Bloom, J. S., et al. 2011, ApJ, 743, 154
- Dai, Z. G., & Lu, T. 2002, ApJ, 565, L87
- Dai, Z. G., & Wu, X. F. 2003, ApJ, 591, L21
- Dai, Z. G., Wang, X. Y., Wu, X. F., & Zhang, B. 2006, Science, 311, 1127
- Daigne, F., & Mochkovitch, R. 1998, MNRAS, 296, 275
- Drenkhahn, G., & Spruit, H. C. 2004, Astronomical Society of the Pacific Conference Series, 312, 357
- Fan, Y. Z., & Wei, D. M. 2005, MNRAS, 364, L42
- Ferrero, P., Kann, D. A., Klose, S., et al. 2008, American Institute of Physics Conference Series, 1000, 257
- Ferrero, P., Klose, S., Kann, D. A., et al. 2009, A&A, 497, 729
- Fynbo, J. P. U., Jakobsson, P., Prochaska, J. X., et al. 2009, ApJS, 185, 526
- Gehrels, N., Chincarini, G., Giommi, P., et al. 2004, ApJ, 611, 1005
- Gendre, B., Klotz, A., Palazzi, E., et al. 2010, MNRAS, 405, 2372
- Giannios, D., & Spruit, H. C. 2006, A&A, 450, 887
- Golenetskii, S., Aptekar, R., Mazets, E., et al. 2006, GRB Coordinates Network, 5837, 1
- Golenetskii, S., Aptekar, R., Mazets, E., et al. 2007, GRB Coordinates Network, 6879, 1
- Gorbovskoy, E. S., Lipunova, G. V., Lipunov, V. M., et al. 2012, MNRAS, 421, 1874
- Granot, J., & Kumar, P. 2003, ApJ, 591, 1086
- Granot, J., Panaitescu, A., Kumar, P., & Woosley, S. E. 2002, ApJ, 570, L61
- Granot, J., Nakar, E., & Piran, T. 2003, Nature, 426, 138
- Granot, J. 2005, ApJ, 631, 1022
- Grupe, D., Gronwall, C., Wang, X.-Y., et al. 2007, ApJ, 662, 443
- Guidorzi, C., Clemens, C., Kobayashi, S., et al. 2009, A&A, 499, 439

- Guidorzi, C., Kobayashi, S., Perley, D. A., et al. 2011, MNRAS, 417, 2124
- He, H.-N., Wu, X.-F., Toma, K., Wang, X.-Y., & Mészáros, P. 2011, ApJ, 733, 22
- Huang, Y. F., Gou, L. J., Dai, Z. G., & Lu, T. 2000, ApJ, 543, 90
- Huang, Y. F., Wu, X. F., Dai, Z. G., Ma, H. T., & Lu, T. 2004, ApJ, 605, 300
- Huang, K. Y., Wang, S. Y., & Urata, Y. 2009, American Institute of Physics Conference Series, 1133, 212
- Jia, L.-W., Wu, X.-F., Lü, H.-J., Hou, S.-J., & Liang, E.-W. 2012, Research in Astronomy and Astrophysics, 12, 411
- Jin, Z. P., Xu, D., Covino, S., et al. 2009, MNRAS, 400, 1829
- Kann, D. A., Klose, S., & Zeh, A. 2006, ApJ, 641, 993
- Kann, D. A., Klose, S., Zhang, B., et al. 2010, ApJ, 720, 1513
- Kann, D. A., Klose, S., Zhang, B., et al. 2011, ApJ, 734, 96
- Kirk, J. G., Guthmann, A. W., Gallant, Y. A., & Achterberg, A. 2000, ApJ, 542, 235
- Klotz, A., Gendre, B., Stratta, G., et al. 2008, A&A, 483, 847
- Klotz, A., Gendre, B., Atteia, J. L., et al. 2009, ApJ, 697, L18
- Kobayashi, S., & Zhang, B. 2007, ApJ, 655, 973
- Kobayashi, S., Piran, T., & Sari, R. 1997, ApJ, 490, 92
- Krühler, T., Greiner, J., Afonso, P., et al. 2009, A&A, 508, 593
- Krühler, T., Greiner, J., McBreen, S., et al. 2009, ApJ, 697, 758
- Krimm, H. A., Yamaoka, K., Sugita, S., et al. 2009, ApJ, 704, 1405
- Kuin, N. P. M., Landsman, W., Page, M. J., et al. 2009, MNRAS, 395, L21
- Laas-Bourez, M., Klotz, A., Coward, D., et al. 2010, GRB Coordinates Network, 11382, 1
- Lazzati, D., Rossi, E., Covino, S., Ghisellini, G., & Malesani, D. 2002, A&A, 396, L5
- Lazzati, D., Covino, S., di Serego Alighieri, S., et al. 2003, A&A, 410, 823
- Li, W., & Filippenko, A. V. 2008, GRB Coordinates Network, 7475, 1



- Li, W., Filippenko, A. V., Chornock, R., & Jha, S. 2003, *ApJ*, 586, L9
- Li, L., Liang, E.-W., Tang, Q.-W., et al. 2012, *ApJ*, 758, 27 (paper I)
- Liang, E., & Zhang, B. 2006, *ApJ*, 638, L67
- Liang, E., Racusin, J. L., Zhang, B., Zhang, B.-B., & Burrows, D. N. 2008, *American Institute of Physics Conference Series*, 1000, 204
- Liang, E.-W., Yi, S.-X., Zhang, J., et al. 2010, *ApJ*, 725, 2209
- Liang, E., & Zhang, B. 2006, *ApJ*, 638, L67
- Littlejohns, O. M., Willingale, R., O’Brien, P. T., et al. 2012, *MNRAS*, 421, 2692
- Liu, X. W., Wu, X. F., & Lu, T. 2008, *A&A*, 487, 503
- Mészáros, P., & Rees, M. J. 1997, *ApJ*, 476, 232
- Mészáros, P., & Rees, M. J. 2003, *ApJ*, 591, L91
- Mészáros, P., Razzaque, S., & Wang, X. Y. 2006, *Particles and Nuclei*, 842, 1007
- Malesani, D., Fynbo, J. P. U., Vreeswijk, P. M., & Villforth, C. 2008, *GRB Coordinates Network*, 7436, 1
- Mao, J., Malesani, D., D’Avanzo, P., et al. 2012, *A&A*, 538, A1
- Margutti, R., Guidorzi, C., Chincarini, G., et al. 2010, *MNRAS*, 406, 2149
- Melandri, A., Guidorzi, C., Kobayashi, S., et al. 2009, *MNRAS*, 395, 1941
- Melandri, A., Kobayashi, S., Mundell, C. G., et al. 2010, *ApJ*, 723, 1331
- Meszáros, P., Rees, M. J., & Wijers, R. A. M. J. 1998, *ApJ*, 499, 301
- Molinari, E., Vergani, S. D., Malesani, D., et al. 2007, *A&A*, 469, L13
- Nakar, E., & Granot, J. 2007, *MNRAS*, 380, 1744
- Nardini, M., Ghisellini, G., Ghirlanda, G., et al. 2006, *A&A*, 451, 821
- Nardini, M., Greiner, J., Krühler, T., et al. 2011, *A&A*, 531, A39
- Page, K. L., Willingale, R., Bissaldi, E., et al. 2009, *MNRAS*, 400, 134
- Panaitescu, A., & Kumar, P. 2001, *ApJ*, 554, 667

- Panaitescu, A., & Vestrand, W. T. 2008, MNRAS, 387, 497
- Panaitescu, A., & Vestrand, W. T. 2011, MNRAS, 414, 3537
- Panaitescu, A., Mészáros, P., & Rees, M. J. 1998, ApJ, 503, 314
- Pandey, S. B., Swenson, C. A., Perley, D. A., et al. 2010, ApJ, 714, 799
- Pe’er, A., Mészáros, P., & Rees, M. J. 2006, ApJ, 642, 995
- Pelassa, V., & Ohno, M. 2010, arXiv:1002.2863
- Perley, D. A., Li, W., Chornock, R., et al. 2008, ApJ, 688, 470
- Perley, D. A., Bloom, J. S., Klein, C. R., et al. 2010, MNRAS, 406, 2473
- Perna, R., Armitage, P. J., & Zhang, B. 2006, ApJ, 636, L29
- Prochaska, J. X., Chen, H.-W., Bloom, J. S., et al. 2007, ApJS, 168, 231
- Proga, D., & Zhang, B. 2006, MNRAS, 370, L61
- Racusin, J. L., Karpov, S. V., Sokolowski, M., et al. 2008, Nature, 455, 183
- Rana, V., Cenko, B., Harrison, F., Fox, D., & Kelemen, J. 2009, American Astronomical Society Meeting Abstracts #213, 213, #610.03
- Rees, M. J., & Mészáros, P. 1994, ApJ, 430, L93
- Rees, M. J., & Mészáros, P. 2005, ApJ, 628, 847
- Rees, M. J., & Meszaros, P. 1992, MNRAS, 258, 41P
- Resmi, L., Ishwara-Chandra, C. H., Castro-Tirado, A. J., et al. 2005, A&A, 440, 477
- Robertson, B. E., & Ellis, R. S. 2012, ApJ, 744, 95
- Rossi, E., Lazzati, D., & Rees, M. J. 2002, MNRAS, 332, 945
- Rossi, A., Schulze, S., Klose, S., et al. 2011, A&A, 529, A142
- Ruiz-Velasco, A. E., Swan, H., Troja, E., et al. 2007, ApJ, 669, 1
- Rykoff, E. S., Smith, D. A., Price, P. A., et al. 2004, ApJ, 601, 1013
- Sakamoto, T., Barthelmy, S. D., Baumgartner, W. H., et al. 2010, GRB Coordinates Network, 11169, 1

- Sari, R., & Piran, T. 1999, *ApJ*, 520, 641
- Sari, R., Piran, T., & Narayan, R. 1998, *ApJ*, 497, L17
- Schady, P., de Pasquale, M., Page, M. J., et al. 2008, *American Institute of Physics Conference Series*, 1000, 200
- Schlegel, D. J., Finkbeiner, D. P., & Davis, M. 1998, *ApJ*, 500, 525
- Shen, R., Kumar, P., & Robinson, E. L. 2006, *MNRAS*, 371, 1441
- Thöne, C. C., Kann, D. A., Jóhannesson, G., et al. 2010, *A&A*, 523, A70
- Thompson, C. 1994, *MNRAS*, 270, 480
- Uehara, T., Uemura, M., Arai, A., et al. 2011, *A&A*, 526, A92
- Uhm, Z. L., Zhang, B., Hascoet, R., et al. 2012, *arXiv:1208.2347*
- Usov, V. V. 1992, *Nature*, 357, 472
- Wren, J., Vestrand, W. T., Wozniak, P. R., Davis, H., & Norman, B. 2009, *GRB Coordinates Network*, 9778, 1
- Wu, X. F., Dai, Z. G., Huang, Y. F., & Lu, T. 2005, *MNRAS*, 357, 1197
- Xue-Wen, L., Xue-Feng, W., & Tan, L. 2009, *arXiv:0907.1767*
- Yost, S. A., Alatalo, K., Rykoff, E. S., et al. 2006, *ApJ*, 636, 959
- Yuan, F., Rykoff, E. S., Schaefer, B. E., et al. 2008, *American Institute of Physics Conference Series*, 1065, 103
- Yuan, F., Schady, P., Racusin, J. L., et al. 2010, *ApJ*, 711, 870
- Zafar, T., Watson, D., Fynbo, J. P. U., et al. 2011, *A&A*, 532, A143
- Zhang, B., & Mészáros, P. 2002, *ApJ*, 571, 876
- Zhang, B., & Mészáros, P. 2002, *ApJ*, 581, 1236
- Zhang, B., & Mészáros, P. 2004, *International Journal of Modern Physics A*, 19, 2385
- Zhang, B., & Yan, H. 2011, *ApJ*, 726, 90
- Zhang, B., Kobayashi, S., & Mészáros, P. 2003, *ApJ*, 595, 950

- Zhang, B., Dai, X., Lloyd-Ronning, N. M., & Mészáros, P. 2004, ApJ, 601, L119
- Zhang, B., Fan, Y. Z., Dyks, J., et al. 2006, ApJ, 642, 354
- Zhang, B., Zhang, B.-B., Liang, E.-W., et al. 2007, ApJ, 655, L25
- Zhang, B. 2007, Chinese J. Astron. Astrophys., 7, 1
- Zhang, B. 2011, Comptes Rendus Physique, 12, 206

Table 1. Parameters of the Onset Bumps

GRB(Band) <sup>ref</sup>	$F_m^a$	$\alpha_1$	$\alpha_2$	$t_p^b$	$w^b$	$t_r^b$	$t_d^b$	$R_{rd}$	$R_{rp}$	$z$	$E_{\gamma,iso}^c$	$E_{R,iso}^d$	$L_{p,R}^e$	$\Gamma_0$	$R_{dec}^f$
030418(V) <sup>(1)</sup>	3.33±0.07	-0.81±0.12	0.55±0.04	1190±109	6015	926	5089	0.18	0.71	...	...	...	...	...	...
050502A(V) <sup>(2)</sup>	55.22±3.56	-0.87	1.30±0.07	58±5	96	34	62	0.55	0.63	3.793 <sup>(36)</sup>	...	162.5	5139.5±331.4	...	...
050820A(R) <sup>(3)</sup>	17.38±0.11	-1.26±0.04	1.07±0.02	477±6	896	258	637	0.41	0.53	2.612 <sup>(36)</sup>	159.2±12.4	301.6	671.7±4.3	400	4.77
060110(V) <sup>(4)</sup>	125.78±1.81	-1.05±0.04	0.77±0.03	50	132	30	101	0.30	0.58	...	3.2±0.6	...	...	353	1.41
060418(H) <sup>(5)</sup>	52.99±1.51	-1.24±0.14	1.27±0.02	170±5	252	85	167	0.51	0.50	1.489 <sup>(37)</sup>	48.6±10.6	200.3	606.4±17.3	441	3.01
060605(R) <sup>(6)</sup>	8.65±0.23	-0.78±0.13	1.47±0.04	590±45	1216	336	880	0.38	0.75	3.78 <sup>(38)</sup>	2.8±0.5	362.3	1277.7±33.2	248	1.71
060607A(H) <sup>(7)</sup>	16.65±0.27	-2.39±0.12	1.40±0.02	179±3	220	65	155	0.42	0.35	3.082 <sup>(39)</sup>	23.4±1.5	202.0	926.9±15.1	476	2.24
060904B(R) <sup>(8)</sup>	8.35±0.16	-2.40±0.18	1.76±0.03	400	616	195	421	0.46	0.45	0.703 <sup>(40)</sup>	0.8±0.1	8.6	19.4±0.4	165	1.45
060906(R) <sup>(9)</sup>	0.37±0.06	-0.55±0.68	1.14±0.34	1149±355	2177	788	1389	0.57	0.76	3.686 <sup>(41)</sup>	17.3±1.4	27.2	23.9±4.0	240	3.19
061007(R) <sup>(6)</sup>	1895.00±34.75	-2.00	1.67	77±1	130	41	90	0.45	0.50	1.261 <sup>(42)</sup>	421.0±41.9	1277.2	14688.1±269.3	750	4.33
061121(V) <sup>(10)</sup>	603.77±35.17	-1.23±0.29	1.07±0.23	208±25	394	114	280	0.41	0.54	1.341 <sup>(43)</sup>	284.7±32.7	830.2	4371.4±254.6	499	4.99
070318(V) <sup>(11)</sup>	16.01±0.52	-0.54±0.11	1.16±0.16	507±46	947	347	600	0.58	0.77	0.836 <sup>(44)</sup>	1.3±0.3	28.7	47.0±1.5	167	1.74
070411(R) <sup>(12)</sup>	2.75±0.05	-0.61	1.45±0.02	739±10	1196	473	723	0.65	0.74	2.954 <sup>(40)</sup>	10.0±2.0	79.8	145.6±2.4	248	2.60
070419A(R) <sup>(13)</sup>	0.45±0.02	-0.93±0.12	1.26±0.03	765±30	1212	437	775	0.56	0.59	0.97 <sup>(40)</sup>	0.2±0.02	1.8	1.9±0.1	115	1.16
070420(R) <sup>(14)</sup>	14.63±1.17	-1.29±0.48	0.90±0.08	202±22	424	107	317	0.34	0.51	...	31.0±5.0	...	...	278	3.52
071010A(R) <sup>(15)</sup>	2.51±0.64	-1.50	1.14±0.04	586±66	996	289	707	0.41	0.48	0.98 <sup>(40)</sup>	0.1±0.01	8.3	10.0±2.5	121	0.99
071010B(R) <sup>(16)</sup>	2.72±0.27	-0.34±0.19	0.60±0.06	287±145	1296	215	1081	0.20	0.91	0.947 <sup>(45)</sup>	1.7±0.9	6.4	6.4±0.6	218	1.58
071025(J) <sup>(17)</sup>	5.75±0.17	-1.17±0.15	1.03±0.04	548±29	1090	309	781	0.40	0.55	5.2 <sup>(40)</sup>	15.0±3.0	...	...	346	2.39
071031(R) <sup>(18)</sup>	0.72±0.0007	-0.63±0.002	0.84±0.0007	1213±2	3312	853	2459	0.35	0.75	2.692 <sup>(40)</sup>	3.9±0.6	40.9	26.9±0.025	179	2.37
071112C(R) <sup>(19)</sup>	2.58±0.14	-1.64±1.18	0.88±0.02	178±13	396	91	306	0.30	0.47	0.823 <sup>(46)</sup>	...	2.1	6.7±0.4	...	2.1
080310(R) <sup>(20)</sup>	1.87±0.11	-1.50	1.16±0.26	184±12	286	85	200	0.43	0.45	2.4266 <sup>(40)</sup>	5.9±1.0	9.9	42.3±2.5	371	1.67
080319A(R) <sup>(21)</sup>	0.18±0.02	-1.80	0.65±0.07	238±17	784	127	657	0.19	0.46	...	8.0±1.0	...	...	221	2.61
080330(R) <sup>(22)</sup>	1.26±0.04	-0.33	1.12±0.25	578±25	1207	395	811	0.49	0.91	1.51 <sup>(40)</sup>	0.4±0.1	10.7	11.4±0.4	154	1.23
080603A(R) <sup>(23)</sup>	0.57±0.03	-1.82±0.21	0.99±0.09	1044±167	6296	1130	5167	0.22	0.70	1.67842 <sup>(47)</sup>	...	...	...	...	...
080710(R) <sup>(19)</sup>	2.59±0.04	-1.60±0.07	1.38±0.06	1934±46	4212	1174	3038	0.39	0.58	0.845 <sup>(40)</sup>	0.8±0.4	23.8	7.9±0.1	95	2.13
080810(R) <sup>(24)</sup>	109.00±1.71	-1.26±0.04	1.21±0.003	117±2	308	78	230	0.34	0.65	3.35 <sup>(40)</sup>	30.0±20.0	836.7	4823.2±75.4	589	2.11
080928(R) <sup>(25)</sup>	2.56±0.18	-0.67±0.11	1.90	2290±155	3017	1388	1629	0.85	0.69	1.692 <sup>(48)</sup>	2.8±0.5	71.2	53.2±3.8	120	2.77
081008(R) <sup>(26)</sup>	6.12±0.08	-2.84±0.16	0.96±0.004	163±2	290	59	230	0.26	0.33	1.967 <sup>(40)</sup>	2.8±0.5	16.9	127.0±1.6	335	1.39
081109A(H) <sup>(27)</sup>	1.04±0.13	-0.19±0.18	0.94±0.03	559±127	1348	344	1005	0.34	0.98	0.98 <sup>(40)</sup>	5.3±0.8	...	...	197	2.46
081126(R) <sup>(28)</sup>	12.30±0.04	-1.14±0.02	0.39±0.01	159±2	1450	127	1323	0.10	0.63	...	9.0±2.0	...	...	260	2.43
081203A(U) <sup>(29)</sup>	146.60±0.30	-2.58±0.02	1.61±0.004	295±2	766	205	561	0.36	0.55	2.1 <sup>(40)</sup>	17.0±4.0	904.0	3022.3±6.2	342	2.51
090102(R) <sup>(30)</sup>	59.05±1.98	-5.22	1.57±0.04	50±1	45	11	34	0.31	0.20	1.547 <sup>(40)</sup>	14.0±5.0	26.6	711.8±23.8	604	1.61
090313(R) <sup>(31)</sup>	6.75±0.43	-1.23±0.16	1.25±0.09	1315±109	2126	690	1436	0.48	0.53	3.375 <sup>(40)</sup>	4.6±0.5	445.7	451.7±28.9	189	2.41
090510(R) <sup>(32)</sup>	0.03±0.003	-0.47±0.14	0.98±0.12	1579±650	5046	853	4194	0.20	0.90	0.903 <sup>(49)</sup>	0.4±0.04	0.3	0.1±0.01	96	1.71
090812(R) <sup>(33)</sup>	14.21±0.87	-1.36±0.32	1.37±0.29	71±8	104	35	69	0.51	0.49	2.452 <sup>(40)</sup>	45.9±6.0	27.6	305.4±18.8	687	2.19
100901A(R) <sup>(34)</sup>	1.45±0.04	-1.87±0.31	1.00±0.10	1260±76	2349	577	1772	0.33	0.43	1.408 <sup>(50)</sup>	2.5	22.2	14.2±0.4	142	2.37
100906A(V) <sup>(34)</sup>	95.73±3.06	-3.40±0.23	1.07±0.02	101±4	245	55	189	0.29	0.43	1.727 <sup>(51)</sup>	...	124.2	936.2±30.0	383	1.22
110205A(R) <sup>(35)</sup>	25.24±0.11	-4.00	1.47±0.00	948±3	971	246	725	0.34	0.24	...	...	...	...	...	...
110213A(V) <sup>(35)</sup>	53.19±2.12	-1.54±0.09	0.91±0.08	293±12	641	153	488	0.31	0.48	1.46 <sup>(52)</sup>	...	...	...	...	...

<sup>a</sup>In units of  $10^{-12}$  erg cm<sup>-2</sup> s<sup>-1</sup>.<sup>b</sup>In units of seconds.<sup>c</sup>In units of  $10^{52}$  erg.<sup>d</sup>In units of  $10^{48}$  erg.<sup>e</sup>In units of  $10^{45}$  erg s<sup>-1</sup>.

<sup>f</sup>In units of  $10^{17} \text{ cm}$ .

References. — (1) Rykoff et al. 2004; (2) Yost et al. 2006; (3) Cenko et al. 2006; (4) Cenko et al. 2008; (5) Molinari et al. 2007; (6) Rykoff et al. 2009 ; (7) Molinari et al. 2007; (8) Klotz et al. 2008; (9) Rana et al. 2009; (10) Uehara et al. 2011; (11) Chester et al. 2008 ; (12) Ferrero et al. 2008; (13) Melandri et al. 2009; (14) Klotz et al 2008. ; (15) Covino et al. 2008; (16) Huang et al.2009; (17) Perley et al. 2009 ; (18) Krühler et al. 2009; (19) Huang et al. 2009; (20) Littlejohns et al.2012; (21) Malesani et al. 2008 ; (22) Guidorzi et al.2009; (23) Guidorzi et al.2011; (24) Page et al.2009; (25) Rossi et al.2010; (26) Yuan et al.2010; (27) Jin et al.2009; (28) Klotz et al.2009; (29) Kuin et al.2009; (30) Gendre et al.2010; (31) Melandri et al.2010; (32) Pelassa et al.2010; (33) Wren et al. 2009(GCN 9778); (34) Gorbovskoy et al.2011; (35) Cucchiara et al.2011; (36) Liang & Zhang. 2006; (37) Prochaska et al.2007; (38) Ferreroet al. 2009; (39) Fynbo et al. 2009; (40) Robertson & Ellis 2012; (41) Zafar et al. 2011; (42) Schady et al. 2008; (43) Golenetskii et al. 2006; (44) Krimm et al. 2009; (45) Golenetskii et al. 2007; (46) Kann et al. 2010; (47) Guidorzi et al. 2011; (48) Zafar et al. 2011; (49) He, Hao-Ning et al. 2011; (50) Sakamoto et al. 2010; (51) Gorbovskoy et al. 2012; (52) Cucchiara et al. 2011.

Table 2. Parameters of the Rebrightening

<i>GRB(Band)</i>	$F_m^a$	$\alpha_1$	$\alpha_2$	$t_p^b$	$w^b$	$t_r^b$	$t_d^b$	$R_{rd}$	$R_{rp}$	$z$	$E_{\gamma,iso}^c$	$E_{R,iso}^d$	$L_{p,R}^e$
021211( <i>R</i> ) <sup>(1)</sup>	281±32	-1.80	0.40±0.06	0.50	3.88	0.31	3.56	0.09	0.50	1.01 <sup>(28)</sup>	111±10	1.4	1.21±0.14
021004( <i>R</i> ) <sup>(2)</sup>	89±5	-2.50	1.27±0.03	170.31±5.31	228.51	62.01	166.49	0.37	0.34	2.335 <sup>(29)</sup>	500±115	373.5	1.80±0.10
030329( <i>R</i> ) <sup>(3)</sup>	1659±198	-2.04±0.54	1.35±0.03	198.55±1.82	265.42	80.05	185.37	0.43	0.39	0.17 <sup>(30)</sup>	155±14	43.1	0.12±0.01
050502 <i>A</i> ( <i>V</i> ) <sup>(4)</sup>	343±140	-0.80	1.40±0.33	2.76±0.72	4.40	1.65	2.74	0.60	0.65	3.793 <sup>(31)</sup>	...	46.3	31.90±13.03
050721( <i>R</i> ) <sup>(5)</sup>	40±1	-0.50	1.06	98.86±7.85	214.89	67.97	146.92	0.46	0.81	...	460±90	0	...
050820 <i>A</i> ( <i>R</i> ) <sup>(6)</sup>	388±22	-0.86±0.27	1.05±0.02	19.39±1.01	39.87	12.09	27.78	0.44	0.65	2.612 <sup>(32)</sup>	15924±1244	287.2	15.00±0.85
060526( <i>R</i> ) <sup>(7)</sup>	59±2	-1.60	2.28	112.46±1.89	104.72	45.73	58.99	0.78	0.42	3.21 <sup>(33)</sup>	606±303	183.7	2.64±0.08
060729( <i>U</i> ) <sup>(8)</sup>	4758±150	-1.20±0.28	1.37±0.06	30.04±2.67	67.93	18.61	49.32	0.38	0.65	0.54 <sup>(29)</sup>	65±5	167.8	5.00±0.16
060904 <i>B</i> ( <i>R</i> ) <sup>(9)</sup>	1655±32	-8.00	0.98±0.02	1.77±0.02	3.46	0.60	2.86	0.21	0.27	0.703 <sup>(30)</sup>	77±10	12.3	3.85±0.08
060906( <i>R</i> ) <sup>(10)</sup>	287±23	-2.91±0.91	1.20	9.72±0.54	13.32	3.28	10.04	0.33	0.31	3.686 <sup>(29)</sup>	1727±139	151.3	18.39±1.46
060927( <i>V</i> ) <sup>(11)</sup>	4203±0	-1.40	1.20	0.48	0.79	0.24	0.55	0.44	0.49	5.6 <sup>(29)</sup>	5815±862	183.8	1095.82
070318( <i>V</i> ) <sup>(12)</sup>	263±662	-0.95±5.14	1.60	52.82±104.81	73.03	29.10	43.93	0.66	0.59	0.836 <sup>(31)</sup>	135±33	38.9	0.77±1.94
071003( <i>R</i> ) <sup>(13)</sup>	992±26	-1.00	1.10	20.00	38.31	11.75	26.56	0.44	0.60	1.605 <sup>(32)</sup>	1800±600	306.1	21.21±0.55
080310( <i>R</i> ) <sup>(14)</sup>	2077±118	-0.51	1.07	1.72±0.06	3.48	1.21	2.28	0.53	0.79	2.4266 <sup>(35)</sup>	590±100	119.0	47.09±2.67
080319 <i>C</i> ( <i>V</i> ) <sup>(15)</sup>	2933±231	-3.40±0.61	0.94±0.05	0.28±0.01	0.56	0.11	0.45	0.25	0.34	1.949 <sup>(29)</sup>	5206±1041	16.5	62.05±4.89
080330( <i>R</i> ) <sup>(16)</sup>	675±148	-1.20	1.14±0.15	1.77±0.10	3.15	0.96	2.19	0.44	0.54	1.51 <sup>(35)</sup>	41±6	15.8	6.12±1.34
080413 <i>A</i> ( <i>R</i> ) <sup>(17)</sup>	23176±1802	-1.00	1.21±0.07	0.15	0.26	0.09	0.17	0.49	0.59	2.433 <sup>(35)</sup>	1855±397	105.6	719.01±55.90
080710( <i>R</i> ) <sup>(18)</sup>	794±45	-0.32±0.05	1.58±0.08	8.63±0.19	13.96	5.90	8.06	0.73	0.90	0.845 <sup>(35)</sup>	80±40	26.4	2.42±0.14
080913( <i>J</i> ) <sup>(19)</sup>	4±1	-2.30	0.95	78.93±33.97	173.07	38.53	134.54	0.29	0.43	6.7 <sup>(35)</sup>	711±89	51.3	1.22±0.48
080928( <i>R</i> ) <sup>(20)</sup>	2318±121	-3.24±0.62	2.22±0.05	7.41±0.25	5.62	1.99	3.63	0.55	0.26	1.692 <sup>(29)</sup>	280±50	140.7	48.09±2.52
081029( <i>R</i> ) <sup>(21)</sup>	771±190	-1.77	1.94±0.11	14.35±0.89	14.57	5.71	8.86	0.64	0.40	3.85 <sup>(33)</sup>	...	462.7	108.26±26.65
090102( <i>R</i> ) <sup>(22)</sup>	90±10	-0.80	0.96±0.02	5.73±0.40	13.19	3.73	9.46	0.39	0.67	1.547 <sup>(35)</sup>	1400±500	8.2	1.08±0.12
090902 <i>B</i> ( <i>R</i> ) <sup>(23)</sup>	15±2	-1.20	0.81	137.28±22.35	360.45	82.29	278.15	0.30	0.56	2.452 <sup>(34)</sup>	4586±597	77.5	0.31±0.05
100219 <i>A</i> ( <i>R</i> ) <sup>(24)</sup>	30±3	-0.91	2.24	20.47±1.08	22.71	10.93	11.79	0.93	0.59	4.6667 <sup>(35)</sup>	...	34.6	1.17±0.10
100901 <i>A</i> ( <i>R</i> ) <sup>(25)</sup>	1633±24	-2.50±0.13	1.50	24.16±0.60	31.58	9.57	22.01	0.43	0.37	1.408 <sup>(36)</sup>	245	371.2	8.26±0.12
101024 <i>A</i> ( <i>R</i> ) <sup>(26)</sup>	164±70	-0.30	1.09±0.11	2.71±1.31	5.78	1.84	3.94	0.47	0.92	...	...	...	...
110213 <i>A</i> ( <i>V</i> ) <sup>(27)</sup>	12064±1159	-1.12±0.19	1.72±0.55	6.14±0.72	7.72	3.12	4.60	0.68	0.53	1.46 <sup>(37)</sup>	...	685.7	65.34±6.28

<sup>a</sup>In units of  $10^{-15}\text{erg cm}^{-2}\text{s}^{-1}$ .<sup>b</sup>In units of kilo seconds.<sup>c</sup>In units of  $10^{50}\text{erg}$ .<sup>d</sup>In units of  $10^{48}\text{erg}$ .<sup>e</sup>In units of  $10^{45}\text{erg s}^{-1}$ .

References. — (1) Li et al.2003; (2) Lazzati et al. 2003; (3) Resmi et al. 2005; (4) Yost et al. 2006; (5) Antonelli et al. 2006; (6) Cenko et al. 2006; (7) Thöne et al.2010; (8) Grupeet et al. 2007 ; (9) Klotz et al.2008; (10) Rana et al. 2009 ; (11) Ruiz-Velasco et al. 2007; (12) Chester et al. 2008 ; (13) Perley et al. 2008; (14) Littlejohns et al. 2012; (15) Li, W. et al.(2008 GCN); (16) Guidorzi et al. 2009 ; (17) Yuan et al. 2008 ; (18) Krühler et al. 2009 ; (19) Xue-Wen, Liu et al. 2009 ; (20) Rossi et al. 2010 ; (21) Nardini et al. 2011 ; (22) Gendre et al. 2010 ; (23) Cenko et al. 2011; (24) Mao et al. 2011; (25) Gorbvskoy et al. 2011; (26) Laas-Bourez et al.(2010 GCN); (27) Cucchiara et al. 2011; (28) Liang & Zhang 2006 (29) Zafar et al. 2011 (30) Robertson & Ellis 2012 (31) Krimm et al. 2009 (32) Krühler et al. 2009 (33) Nardini, M.et al. 2011 (34) Pandey et al. 2010 (35) Mao et al. 2012 (36) Sakamoto et al. 2010 (37) Cucchiara et al. 2011

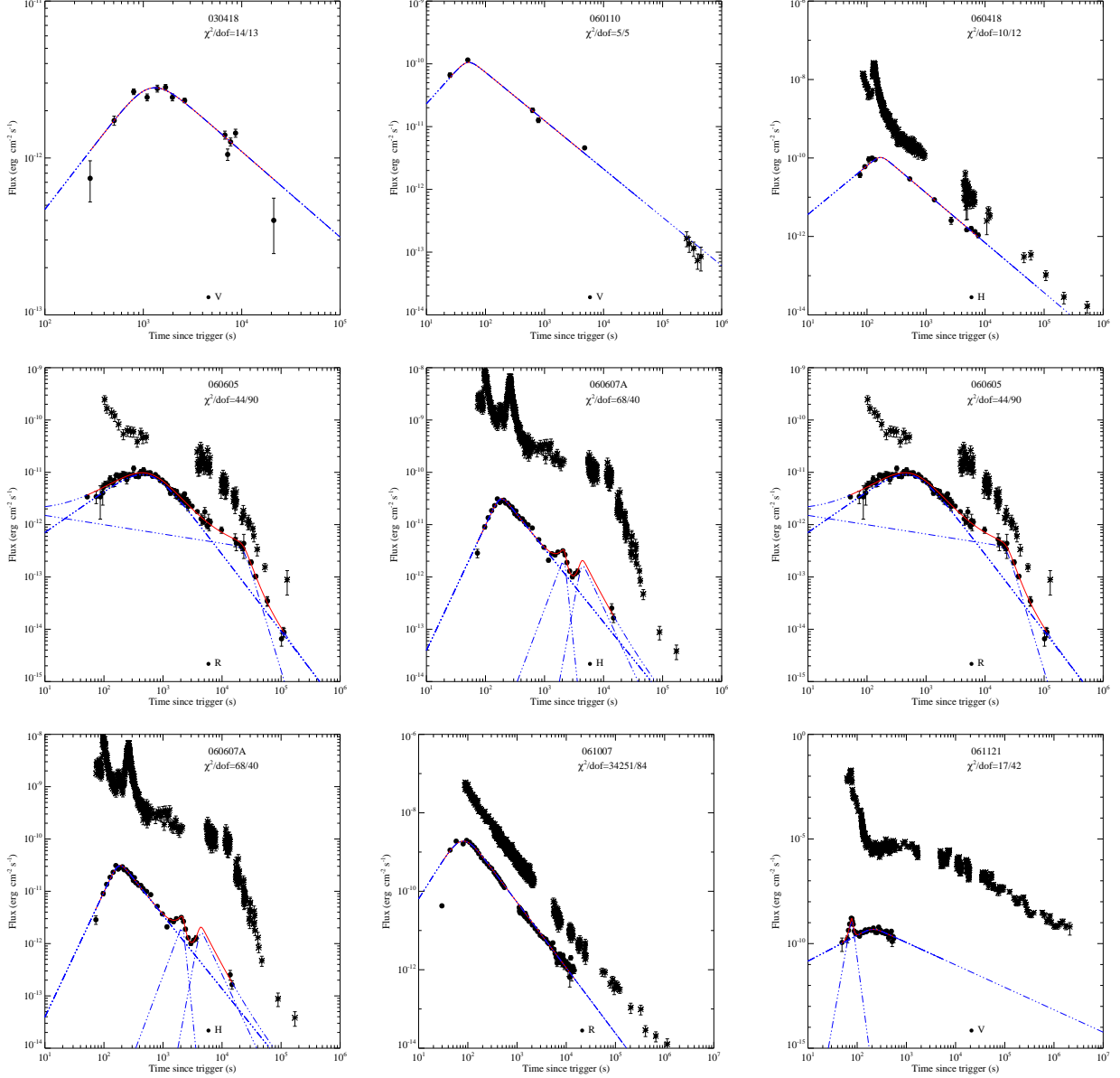


Fig. 1.— Observed optical afterglow lightcurves as predicted by the standard fireball model. Erratic flares are detected in some GRBs. The solid line in each panel is the best fit with our multi-component power-law model. The dashed or dash-dotted lines mark components in the model. The simultaneous X-ray data observed with *Swift*/XRT (crosses with error bands) are also present.



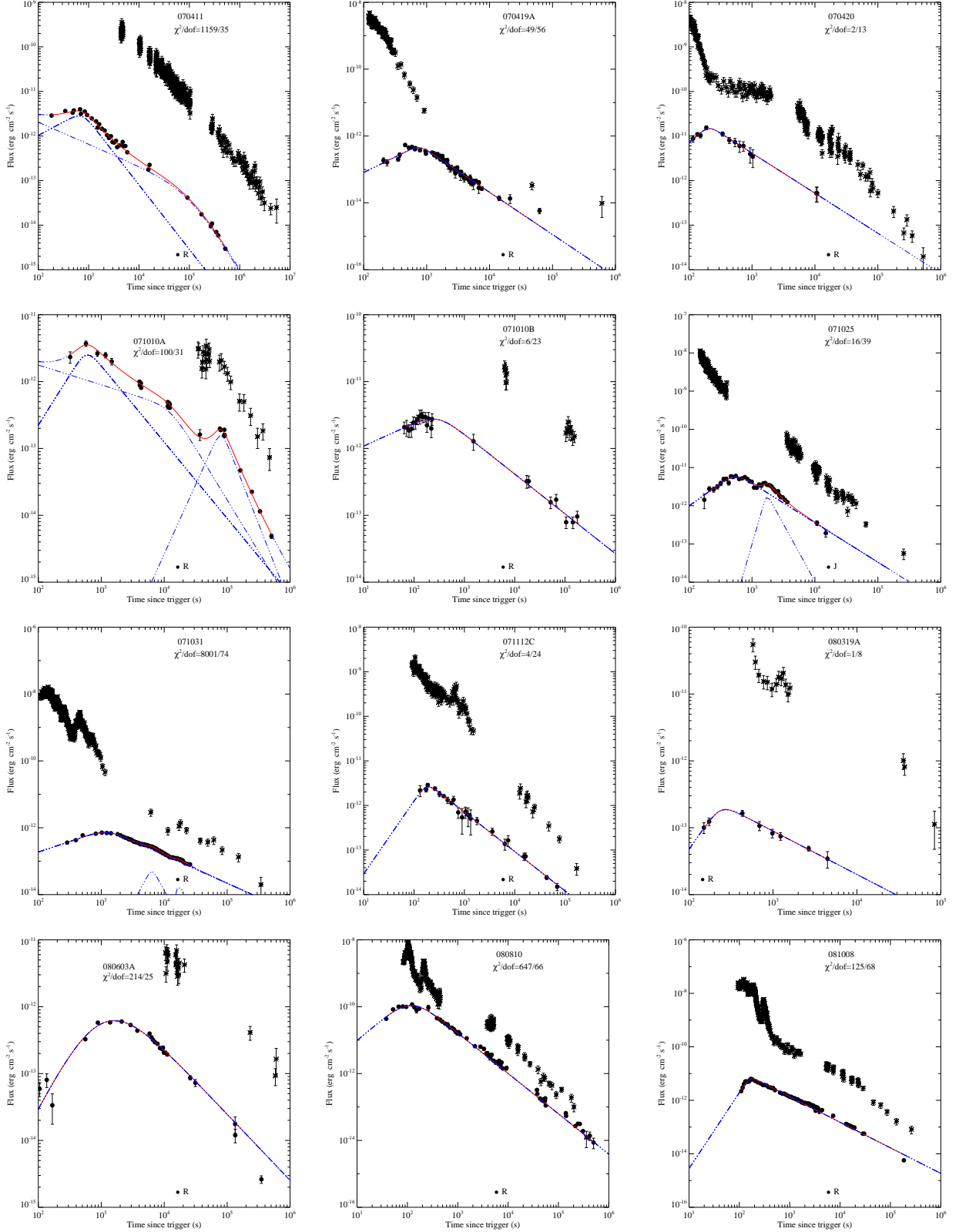


Fig. 1— Continued

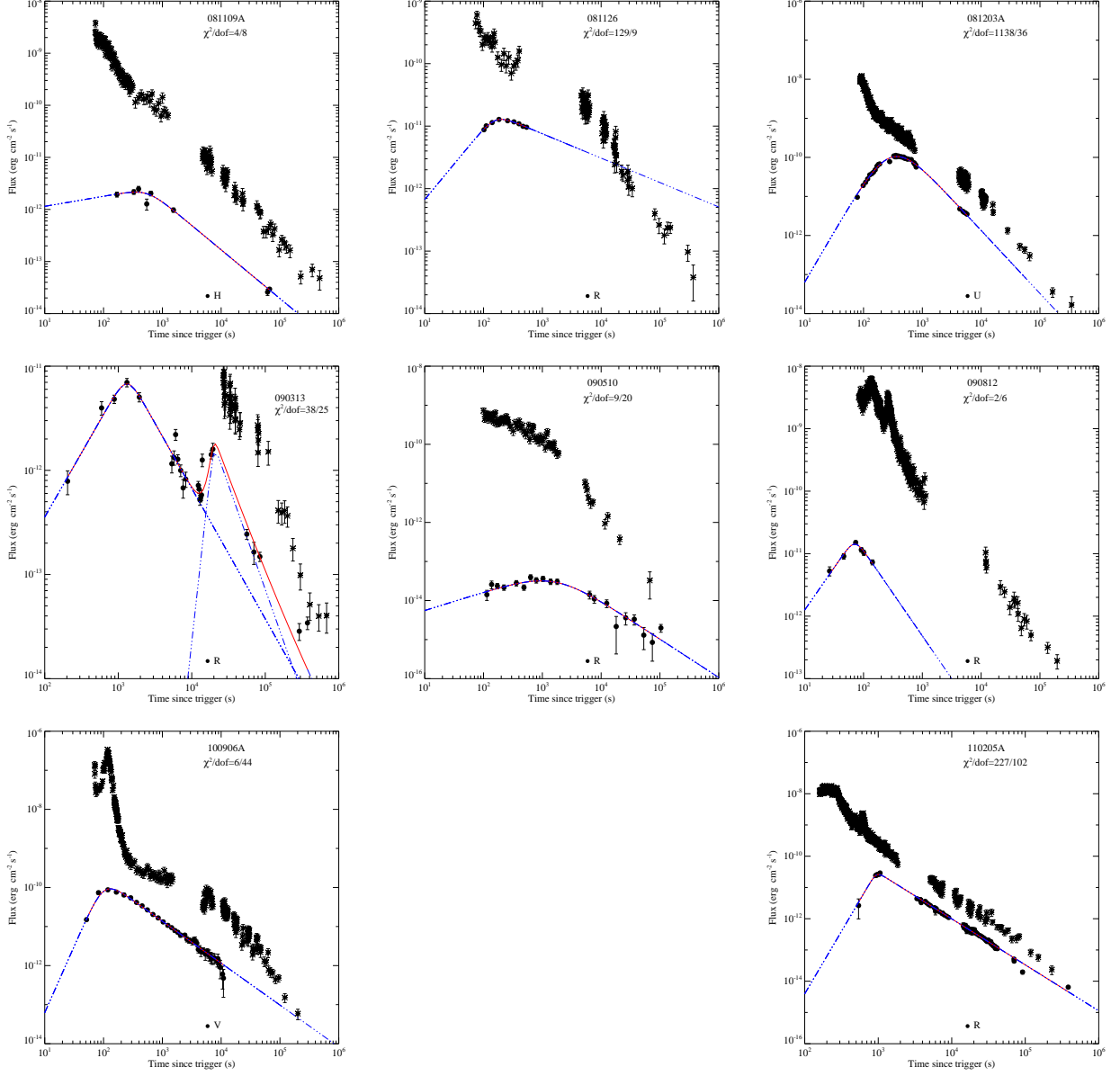


Fig. 1— Continued

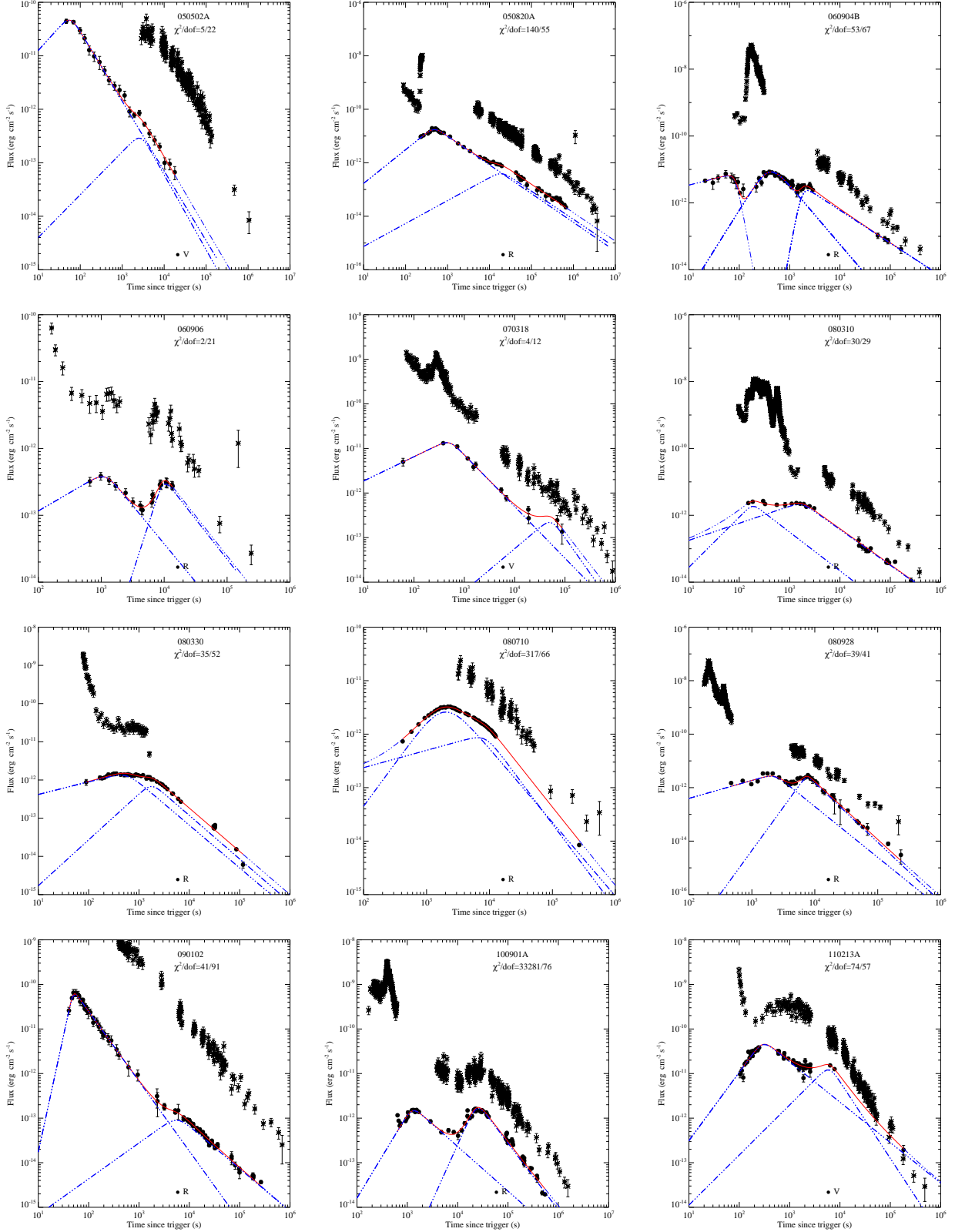


Fig. 2.— Optical lightcurves with detections of both an initial afterglow onset bump and a late re-brightening hump(s). The symbols and line styles are the same as Figure 1.

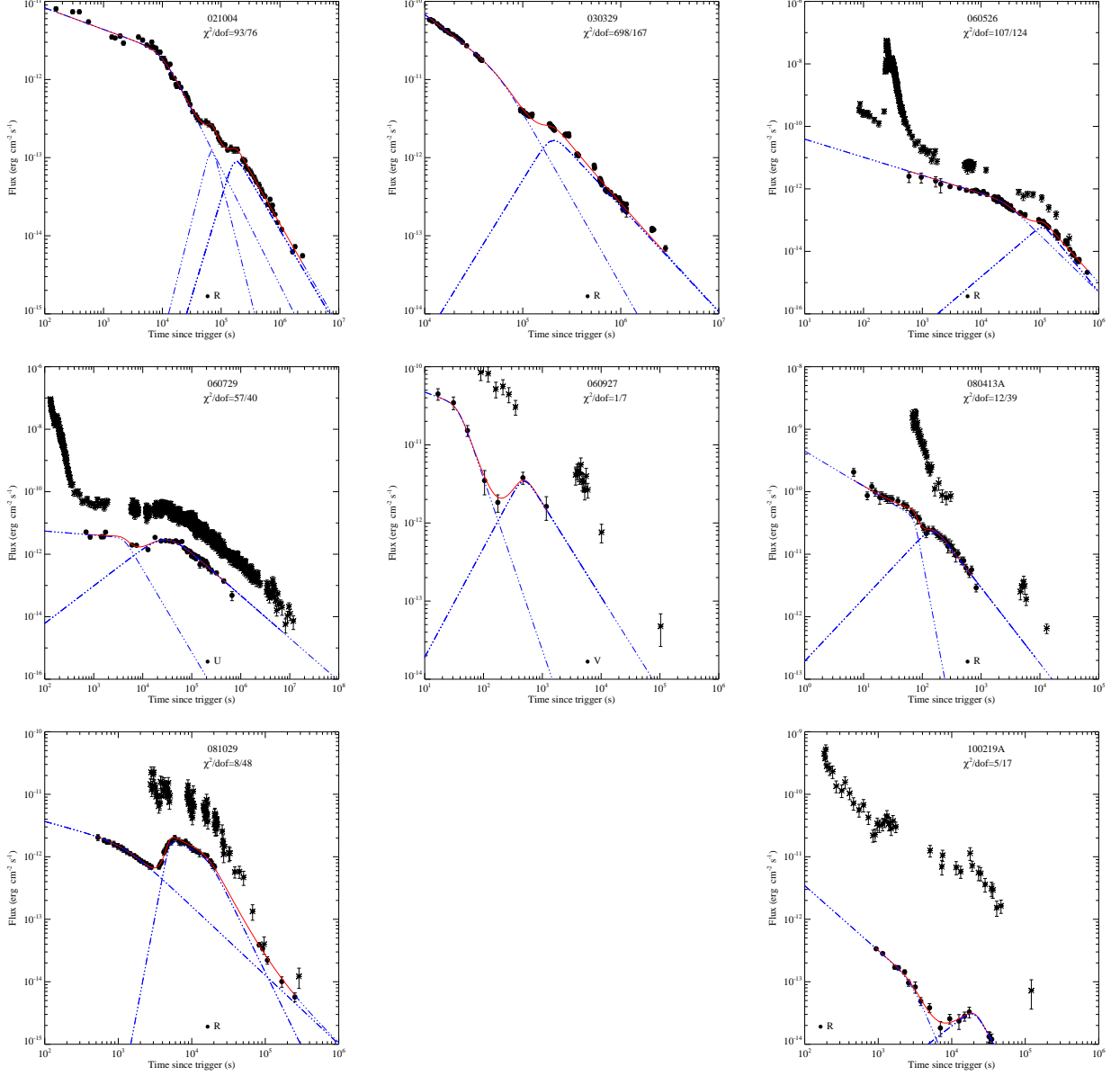


Fig. 3.— Optical lightcurves with detections of both an initial shallow decay segment and a late a late re-brightening hump(s). The symbols and line styles are the same as Figure 1.

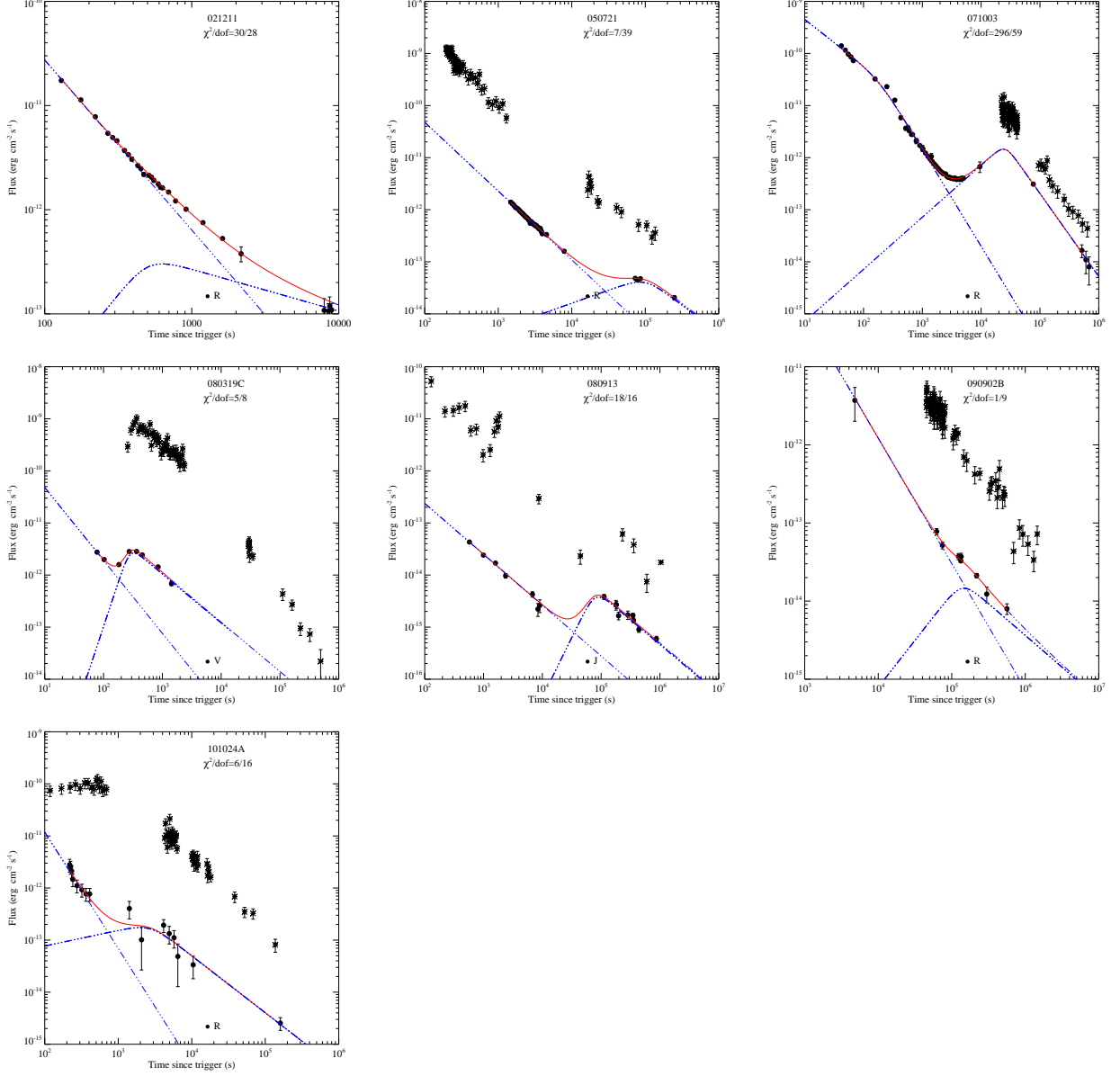


Fig. 4.— Optical lightcurves with detections of both an initial normal decay segment and a late a late re-brightening hump(s). The symbols and line styles are the same as Figure 1.

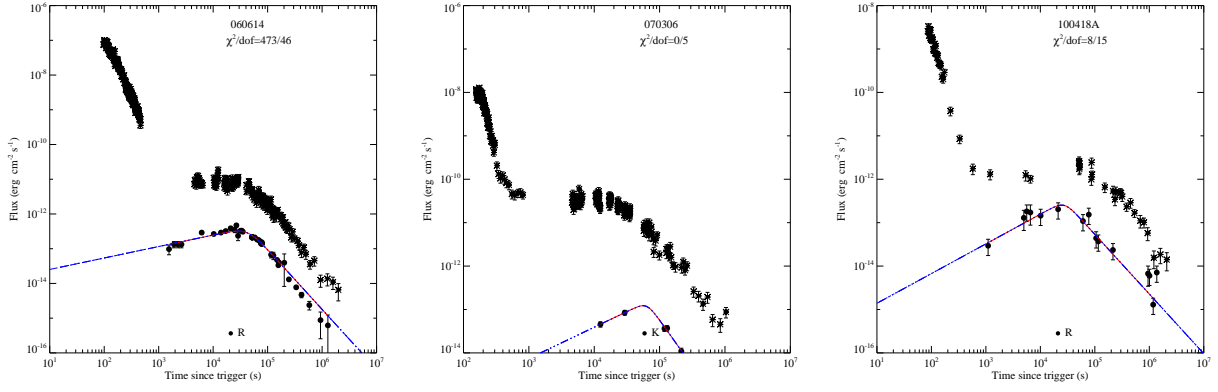


Fig. 5.— Optical lightcurves with detection of a late bump peaking at  $> 10^4$  seconds post the GRB trigger. The symbols and line styles are the same as Figure 1.

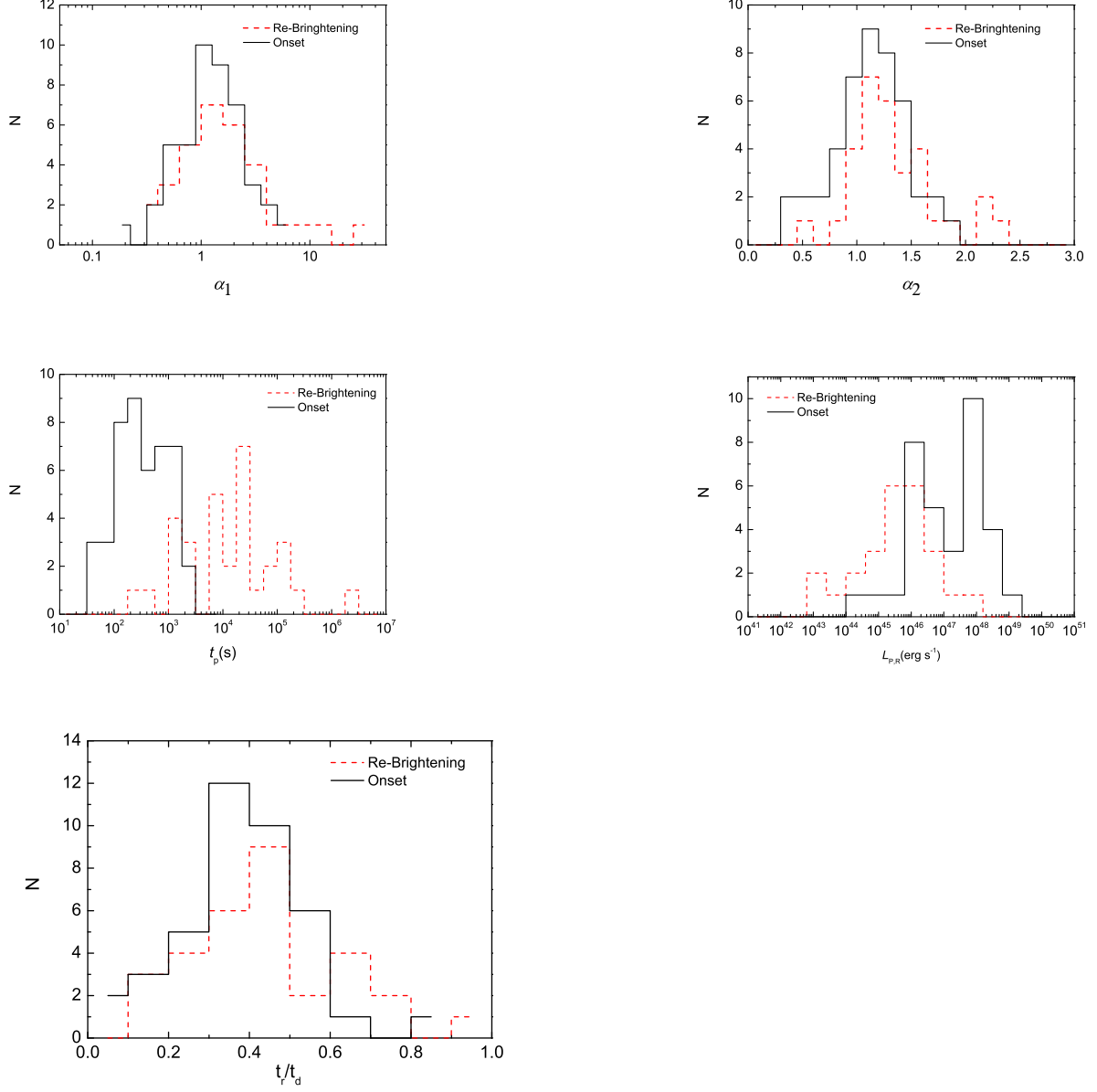


Fig. 6.— Distributions of the characteristics of the re-brightening sample.

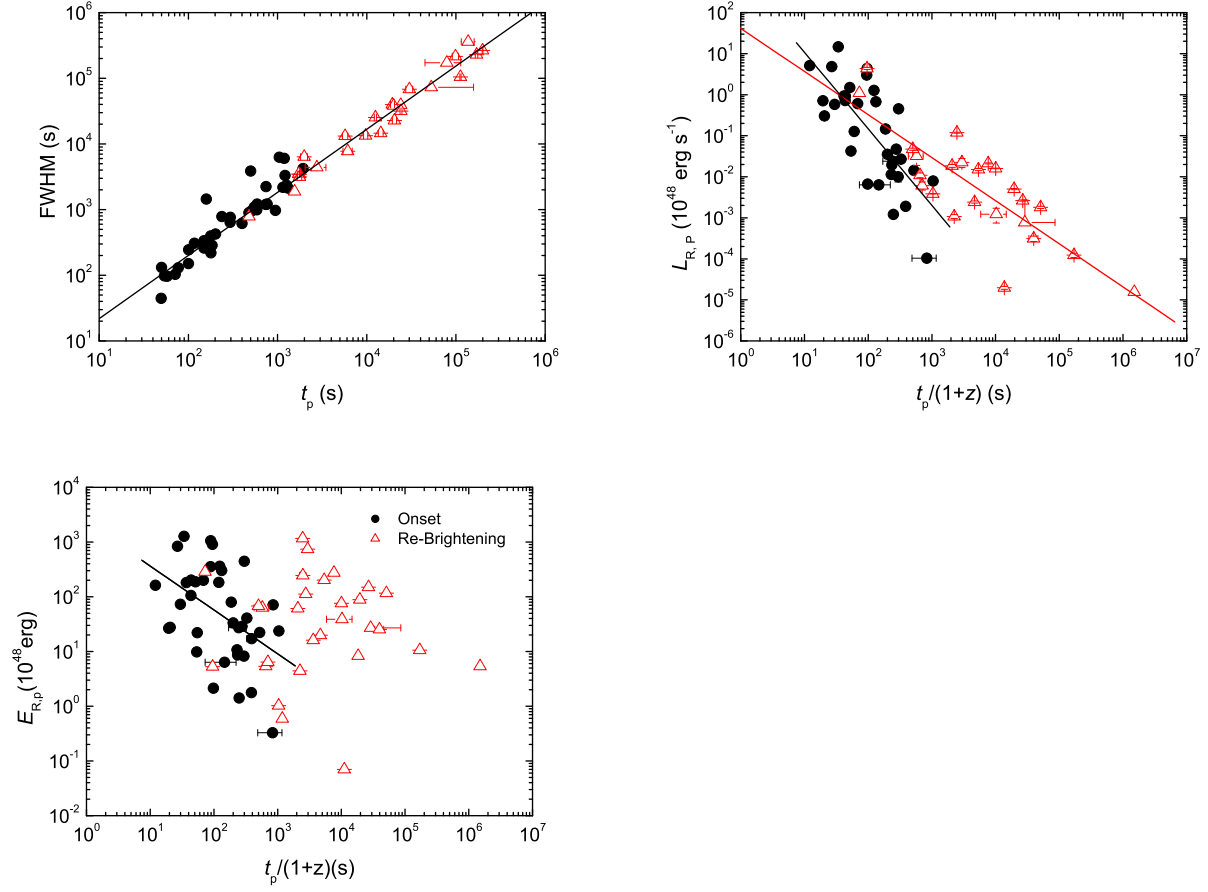


Fig. 7.— Width and peak luminosity as a function of the peak time for the afterglow onset (black solid dots) and re-brightening (open triangles) humps. Lines are the best fits.



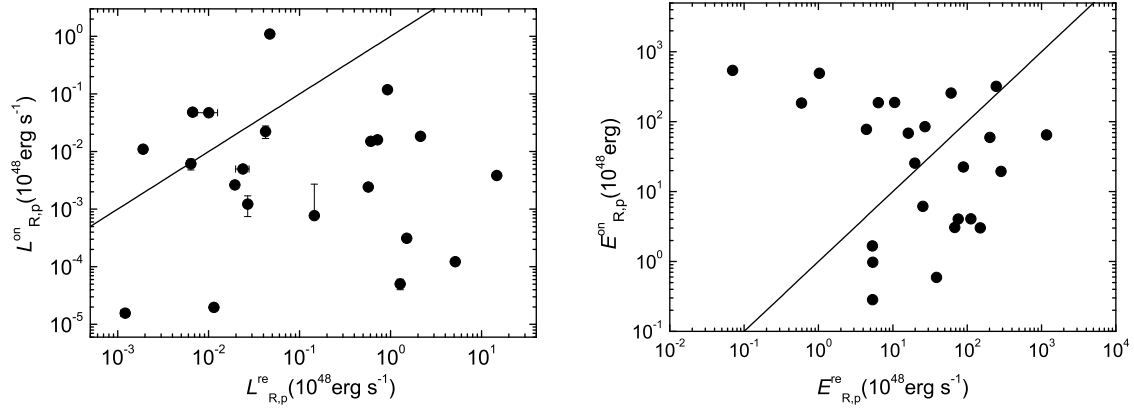


Fig. 8.— Relations of  $L_{P,R}$  between Onset and Re-Brightening sample. Lines are the best fits.

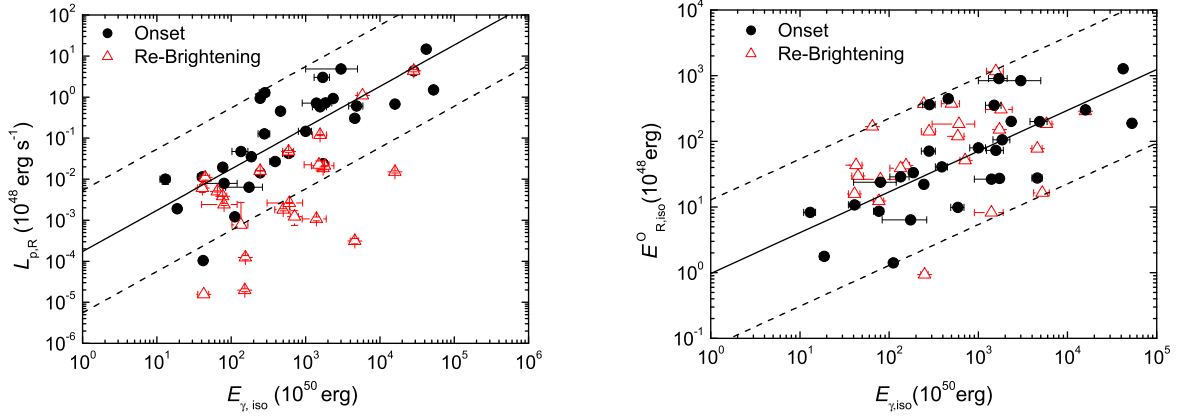


Fig. 9.— Correlation between the peak luminosity the isotropic gamma-ray energy for the afterglow onset (black solid dots) and re-brightening (open triangles) humps .

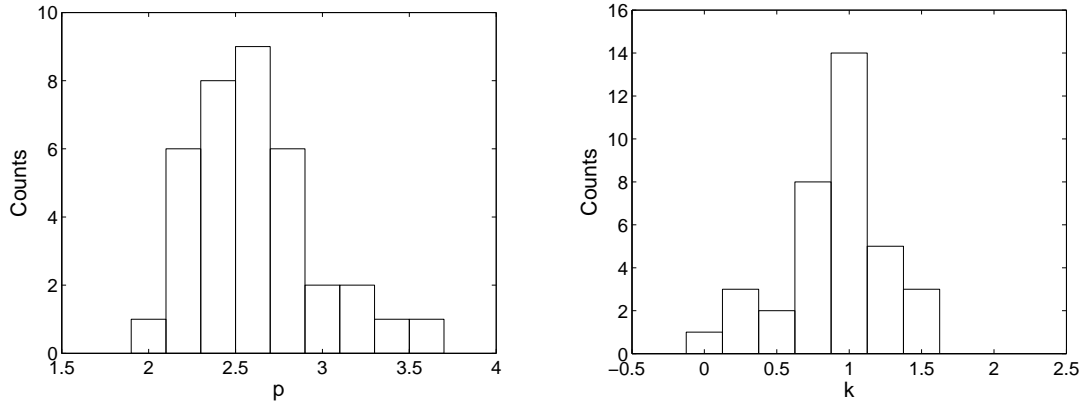


Fig. 10.— Distributions of electron distribution index  $p$  (*left*) and the ambient density profile index  $k$  (*right*) from our sample

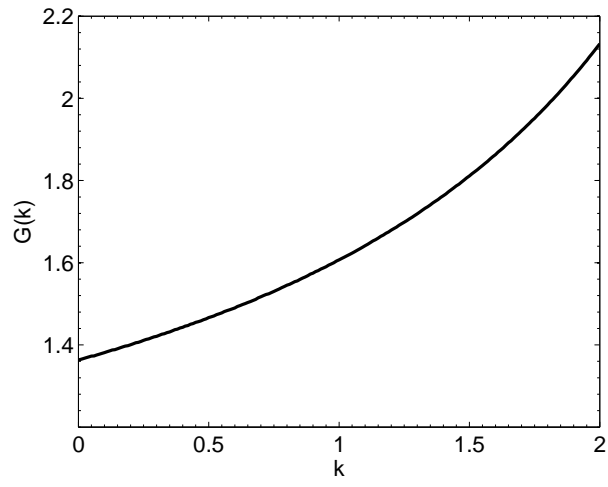


Fig. 11.— The dimensionless  $G(k)$  as a function of  $k$ .

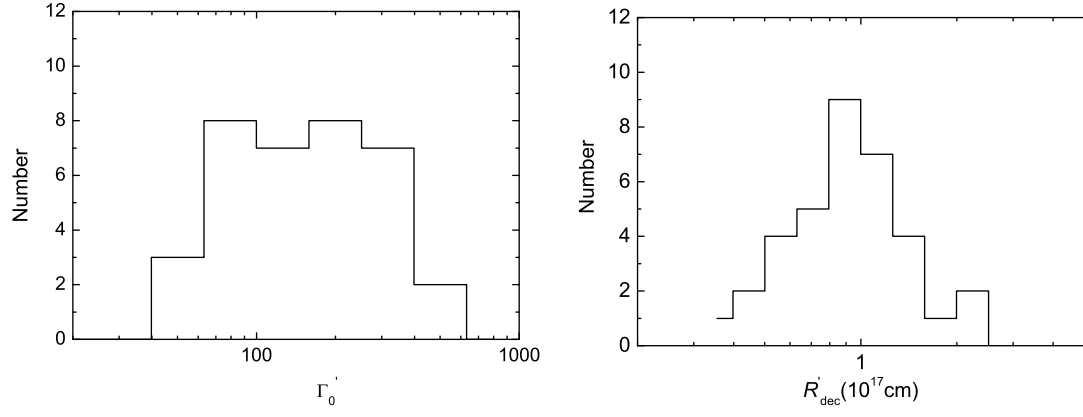


Fig. 12.— The Distributions of  $\Gamma_0'$  and  $R'_{\text{dec}}$

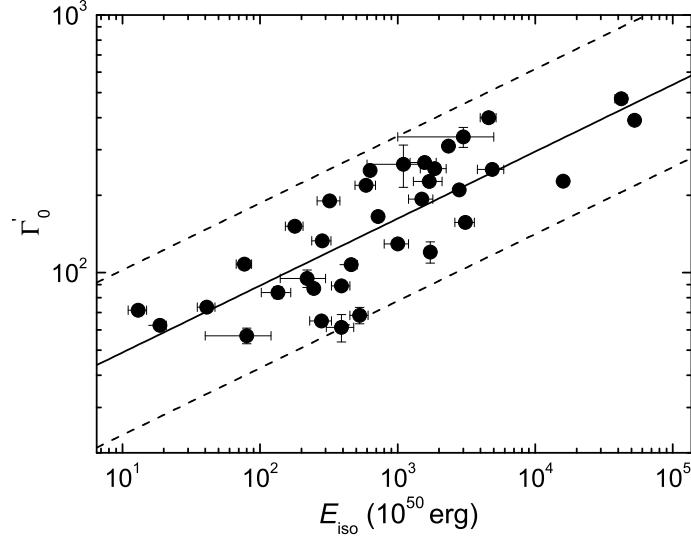


Fig. 13.— The relation between  $\Gamma_0'$  and  $E_{\text{iso}}$ . The solid line is the linear fit to the data and the dashed line mark the scatter of the data in a  $2\sigma$  region.